



Simulation of viscoelastic two-phase flows with insoluble surfactants

Jagannath Venkatesan*, Adhithya Padmanabhan, Sashikumaar Ganesan

Computational Mathematics Group, Department of Computational and Data Sciences, Indian Institute of Science, Bangalore 560012, India

ARTICLE INFO

Keywords:

Viscoelastic fluids
Giesekus model
Insoluble surfactants
Finite elements
ALE approach
Local projection stabilization

ABSTRACT

A stabilized finite element scheme is developed for computations of buoyancy driven 3D-axisymmetric viscoelastic two-phase flows with insoluble surfactants. The numerical scheme solves the Navier–Stokes equations for the fluid flow, Giesekus constitutive equation for the effects of viscoelasticity and simultaneously an evolution equation for the surfactant concentration on the interface. The interface is tracked by the coupled arbitrary Lagrangian–Eulerian (ALE) and Lagrangian approach. The interface-resolved moving meshes allow accurate incorporation of the interfacial tension force, Marangoni forces and the jumps in the material properties. Further, the tangential gradient operator technique is used to handle the curvature approximation in a semi-implicit manner. An one-level Local Projection Stabilization (LPS), which is based on an enriched approximation space and a discontinuous projection space, where both spaces are defined on a same mesh is used to stabilize the model equations. The stabilized numerical scheme allows us to use isoparametric second order conforming finite elements enriched with cubic bubble functions for velocity and viscoelastic stress, second order finite elements for surfactant concentration and discontinuous first order finite element for pressure. A number of computations are performed for a Newtonian drop rising in a viscoelastic fluid column and a viscoelastic drop rising in a Newtonian fluid column with insoluble surfactants on the interface. The influence of the Marangoni number, initial surfactant concentration and Peclet number on the dynamics of the rising drop are analyzed. The numerical study shows that a viscoelastic drop rising in a Newtonian fluid column develops an indentation around the rear stagnation point with a dimpled shape without insoluble surfactants. The presence of insoluble surfactants forces the drop to rise slowly but the drop at the tail end is pulled up more. However, a Newtonian drop rising in a viscoelastic fluid column experiences an extended trailing edge with a cusp-like shape without insoluble surfactants. The presence of surfactants pulls the tail end of the drop up slightly and makes the tail flatter with/without small undulations depending on the magnitude of the surfactant concentrations.

1. Introduction

Surfactants, also known as surface active agents are widely used in numerous scientific, engineering and biomedical applications such as enhanced oil recovery, drug delivery, flow-focusing devices, lung mechanics, polymer blending and plastic production. Surfactants can play an important role in several physical phenomena such as vortex pair interaction, fingering, tip-streaming, drop break-up and coalescence. The presence of insoluble surfactants on the interface between two immiscible liquids alters the flow dynamics significantly. Precisely, surfactant molecules effectively act as a buffer zone between smaller fluid molecules on either side of the interface, altering the strength of the intermolecular forces and thereby lowering the surface tension by an amount that depends on the local surfactant concentration. The transport of surfactants along the interface depends on the local flow behaviour and thus, it results in non-homogeneous distribution of surfactant along the interface. The non-uniform surfactant concentration

induces gradients in interfacial tension, which again gives rise to tangential forces along the interface through the Marangoni convection. In addition to the presence of insoluble surfactants, viscoelasticity plays a prominent role in the aforementioned applications. The fundamental understanding of the simultaneous effects of viscoelasticity and surfactants in multiphase flows is crucial as these effects directly impact the design and optimization of engineering processes subjected to complex interfacial flow dynamics, especially in the field of enhanced oil recovery [1–3]. Therefore, scientific studies on a single drop rising in a fluid column due to buoyancy with viscoelastic and surfactant effects are highly demanded.

Mathematical model describing interfacial flows with viscoelastic effects consist of the Navier–Stokes equations and a viscoelastic constitutive equation. Oldroyd-B [4], Giesekus [5], finitely extensible nonlinear elastic (FENE-P [6], FENE-CR [7]), Phan-Thien-Tanner (PTT) [8] and eXtended Pom-Pom (XPP) [9] are the commonly used constitutive models in the literature for simulating viscoelastic flows. In this

* Corresponding author.

E-mail addresses: jagannathv@iisc.ac.in (J. Venkatesan), adhithyap@iisc.ac.in (A. Padmanabhan), sashi@iisc.ac.in (S. Ganesan).

<https://doi.org/10.1016/j.jnnfm.2019.04.002>

Received 3 July 2018; Received in revised form 4 April 2019; Accepted 7 April 2019

Available online 8 April 2019

0377-0257/© 2019 Elsevier B.V. All rights reserved.

Nomenclature

α	Giesekus mobility factor
β	Newtonian solvent ratio
Γ_{Axial}	Symmetry of axis
Γ_D	Dirichlet boundary
Γ_F	Interface between two liquids
$\hat{\Gamma}_F$	Reference domain for interface
Γ_N	Neumann boundary
δt	Time step length
ε	Ratio between total viscosity of outer and inner phases
k	Sum of principal curvatures
k_h	Fluctuation operator
λ	Relaxation time of polymers
μ_0	Total dynamic viscosity
μ_s	Newtonian solvent viscosity
\mathbf{v}_F	Unit outward normal vector on interface
\mathbf{v}_N	Unit outward normal vector on Neumann boundary
π_h	Global projection operator
π_K	Local projection operator
ρ	Density of fluid
σ_{ref}	Interfacial tension corresponding to reference surfactant concentration
$\boldsymbol{\tau}_N$	Unit tangential vector on Neumann boundary
$\boldsymbol{\tau}_p$	Viscoelastic conformation stress
ϕ	Surfactant concentration space test function
Ψ	Viscoelastic stress space test function
Ω	Computational domain
Ω_0	Initial computational domain
Ω_1	Inner fluid computational domain
Ω_2	Outer fluid computational domain
$\hat{\Omega}$	Reference computational domain
\mathcal{T}_h	Computational mesh
\mathbb{D}	Deformation tensor
\mathbb{I}	Identity tensor
$\mathbb{P}_{\mathbf{v}_F}$	Projection operator onto the tangential plane of Γ_F
\mathbb{S}_{Γ_F}	Interface stress tensor
\mathbb{T}	Stress tensor of fluid
$\nabla_{\Gamma_{\mathbf{v}_F}}$	Interface gradient operator on Γ_F
id	Identity mapping
tr	Trace
Fr	Froude number
Pe	Peclet number
Re	Reynolds number
We	Weber number
Wi	Weissenberg number
g	Gravitational constant
h_c	Height of bulk fluid column
h_K	Diameter of a cell
h_0	Initial mesh size
p	Pressure
q	Pressure space test function
t	Time
C	Surfactant concentration
C_0	Initial surfactant concentration
C_∞	Characteristic surfactant concentration
C_{ref}	Reference surfactant concentration
D	Diameter of the drop at $t = 0$
$D _{r=0}$	Diameter of the drop at the symmetry axis
D_h	Discontinuous projection space
D_s	Surfactant diffusivity
E	Marangoni number
$E_{elastic}$	Elastic energy in the drop

$E_{kinetic}$	Kinetic energy in the drop
G	Surfactant concentration space
K	Cell
\hat{K}	Reference cell
I	Given end time
L	Characteristic length
Q	Pressure space
R	Gas constant
S	Viscoelastic stress space
T	Absolute temperature
U	Velocity along interface
U_∞	Characteristic velocity
V	Velocity space
Y_h	Approximation space
\mathbf{e}	Unit vector in the direction of gravitational force
\mathbf{u}	Fluid velocity
\mathbf{v}	Velocity space test function
\mathbf{w}	Domain velocity

study, we consider the Giesekus constitutive model as it models shear-thinning and elasticity together. In addition, one needs to solve the surface convection-diffusion equation [10,11] for the surfactant concentration on the interface.

Simulation of viscoelastic two-phase flows with insoluble surfactants is a challenging problem in computational rheology. An accurate tracking/capturing of the moving interface is extremely important as the solution of surface convection-diffusion equation for the surfactant concentration depends on the precise position of the interface. Further, the numerical scheme should be able to handle jumps in the material properties (viscosity, density, relaxation time of polymers) across the interface. Moreover, precise inclusion of the interfacial tension force, Marangoni effects and the local curvature on the interface is challenging. In addition, the scheme should be free from spurious velocities and should conserve both the fluid and surfactant mass well. The presence of viscoelasticity in the fluid increases the complexity. At high Weissenberg numbers, the constitutive equation is highly advection dominated which may induce both global and local oscillations in the numerical solution. It necessitates the use of an accurate and robust stabilized numerical scheme to avoid oscillations in the numerical solution.

A number of numerical schemes based on the popular interface capturing/ tracking methods such as volume-of-fluid [12,13], level set [14], front-tracking [15,16], boundary integral [17–19], immersed boundary [20–22], diffuse interface [23,24], arbitrary Lagrangian–Eulerian [25], embedded boundary [26,27] and hybrid [28,29] methods have been proposed in the literature for interfacial flows with surfactants. Also, a meshfree smoothed-particle hydrodynamics method [30] has been used for computations of interfacial flows with surfactants. In the context of interfacial flows with viscoelastic effects, numerous numerical schemes based on volume-of-fluid [31–33], level set [34,35], phase-field [36–38], front-tracking [39–44], arbitrary Lagrangian–Eulerian [45] and boundary integral [46,47] methods have been proposed in the literature. However, to the best of the authors’ knowledge, numerical studies on interfacial flows with simultaneous effects of viscoelasticity and insoluble surfactants has never been reported in the literature.

In this paper, we present an accurate and efficient sharp interface numerical method based on the coupled arbitrary Lagrangian–Eulerian (ALE) and Lagrangian approach for computations of a buoyancy driven 3D-axisymmetric drop rise in a fluid column with simultaneous effects of viscoelasticity and insoluble surfactants. The ALE approach is used for the Navier–Stokes and viscoelastic Giesekus constitutive equations, whereas for the surface convection-diffusion equation we use the Lagrangian approach. Since the interface is resolved by a moving mesh, the collection of edges and cells which approximate the

interface can be used at the same time as the computational domain for the surface convection-diffusion equation. Further, the interfacial force and the different material properties in both the phases can be included very accurately in the ALE approach. Moreover, the spurious velocities which might arise due to the approximation errors of the pressure and the interfacial force, can be suppressed by using this approach [48]. Further, we replace the curvature by the tangential gradient operator and apply integration by parts to reduce one order of differentiation associated with the curvature. This technique allows to treat the curvature term semi-implicitly. Several stabilization schemes such as the Streamline Upwind Petrov Galerkin (SUPG) [49], Discrete Elastic Viscous Stress Splitting (DEVSS) [50,51], Discontinuous Galerkin (DG) [52], Galerkin Least Squares [53], Log-Conformation reformulation [54] and Variational Multiscale [55,56] methods have been proposed in the literature for simulation of viscoelastic fluid flows. Recently, a three-field Local Projection Stabilized (LPS) finite element scheme for simulation of viscoelastic fluid flows in fixed domains has been presented by Venkatesan and Ganesan [57]. In this work, we extend the LPS scheme proposed in [57] for simulation of 3D-axisymmetric viscoelastic two-phase flows with insoluble surfactants. In particular, Local Projection Stabilization is used to handle the convective nature of the viscoelastic constitutive equation and to use equal order interpolation spaces for the velocity and the viscoelastic stress.

The paper is organized as follows. In Section 2, we present the non-dimensional form of the governing equations for buoyancy driven viscoelastic two-phase flows with insoluble surfactants. The coupled ALE–Lagrangian approach, variational form, stabilized finite element formulation, temporal discretization and linearization strategy are described in Section 3. Section 4 presents the numerical results. First, a grid independence test is performed. Then, the numerical scheme is validated by comparison with the numerical results in the literature. Further, a numerical investigation on the viscoelastic drop rising in a Newtonian fluid column and then a Newtonian drop rising in a viscoelastic fluid column with insoluble surfactants on the interface is presented. We examine the influence of the Marangoni number, initial surfactant concentration and Peclet number on the rising drop dynamics. Finally, a brief summary of the proposed numerical scheme and the key observations are presented in Section 5.

2. Mathematical model

2.1. Model problem

A buoyancy driven two-phase viscoelastic flow (either phase can be viscoelastic) in a bounded domain $\Omega \subset \mathbb{R}^3$ with insoluble surfactants on the interface between two liquids is considered. A schematic representation of the computational model is presented in Fig. 1. We assume that a liquid droplet filling $\Omega_1(t)$ is completely surrounded by another liquid filling the domain $\Omega_2(t)$ and the interface between the two liquids is denoted by $\Gamma_F(t)$. Thus, the computational domain is given by $\Omega(t) := \Omega_1(t) \cup \Gamma_F(t) \cup \Omega_2(t)$. Here, t is the time in a given time interval $[0, I]$ with an end time I . Further, Γ_{Axial} , Γ_D , Γ_N and h_c denote the symmetry of axis, Dirichlet, Neumann boundaries and height of the bulk fluid column respectively.

2.2. Governing equations

We assume that the viscoelastic fluid is incompressible, immiscible and the material properties such as density, viscosity and relaxation time of polymers are constant. The fluid flow in $\Omega(t)$ is described by the time-dependent incompressible Navier–Stokes equations, whereas the temporal evolution of viscoelastic stresses in the fluid is described by the Giesekus constitutive equation. Detailed description of the mathematical model without insoluble surfactants on the interface have been presented in our previous study [45], whereas a brief description of the

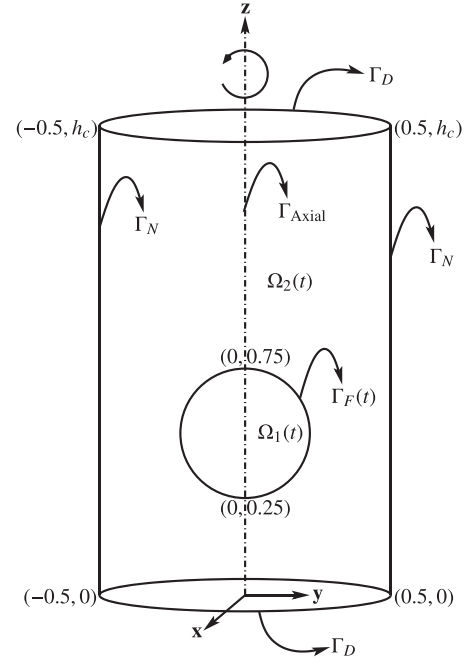


Fig. 1. Computational model of buoyancy driven two-phase viscoelastic flow with insoluble surfactants on the interface.

model and the numerical scheme are presented here. Let

$$x = \frac{\tilde{x}}{L}, \quad \mathbf{u} = \frac{\tilde{\mathbf{u}}}{U_\infty}, \quad \mathbf{w} = \frac{\tilde{\mathbf{w}}}{U_\infty}, \quad t = \frac{\tilde{t} U_\infty}{L}, \quad p = \frac{\tilde{p}}{\rho_2 U_\infty^2},$$

$$I = \frac{\tilde{I} U_\infty}{L}, \quad \boldsymbol{\tau}_p = \tilde{\boldsymbol{\tau}}_p, \quad C = \frac{\tilde{C}}{C_\infty}, \quad \varepsilon = \frac{\mu_{0,2}}{\mu_{0,1}},$$

be the dimensionless length x , fluid velocity \mathbf{u} , domain velocity \mathbf{w} , time t , pressure p , given end time I , viscoelastic conformation stress $\boldsymbol{\tau}_p$, surfactant concentration C and viscosity ratio ε , respectively. Moreover, the tilde over the variables indicate its dimensional form. Here, L , U_∞ and C_∞ are the characteristic length, velocity and surfactant concentrations, respectively. Further, we define the non-dimensional density ρ , Newtonian solvent ratio β , Giesekus mobility factor α , Weissenberg number Wi , Reynolds number Re and Froude number Fr in different parts of the computational domain as

$$\rho = \begin{cases} \rho_1/\rho_2 & \forall \mathbf{x} \in \Omega_1(t), \\ 1 & \forall \mathbf{x} \in \Omega_2(t), \end{cases} \quad \beta = \begin{cases} \beta_1 = \mu_{s,1}/\mu_{0,1} & \forall \mathbf{x} \in \Omega_1(t), \\ \beta_2 = \mu_{s,2}/\mu_{0,2} & \forall \mathbf{x} \in \Omega_2(t), \end{cases}$$

$$\alpha = \begin{cases} \alpha_1 & \forall \mathbf{x} \in \Omega_1(t), \\ \alpha_2 & \forall \mathbf{x} \in \Omega_2(t), \end{cases} \quad Wi = \begin{cases} Wi_1 = \lambda_1 U_\infty/L & \forall \mathbf{x} \in \Omega_1(t), \\ Wi_2 = \lambda_2 U_\infty/L & \forall \mathbf{x} \in \Omega_2(t), \end{cases}$$

$$Re = \begin{cases} \varepsilon Re_2 & \forall \mathbf{x} \in \Omega_1(t), \\ Re_2 & \forall \mathbf{x} \in \Omega_2(t), \end{cases} \quad Re_2 = \frac{\rho_2 U_\infty L}{\mu_{0,2}}, \quad Fr = \frac{U_\infty^2}{Lg}.$$

Here, g is the gravitational constant, ρ_k is the density of fluid, $\mu_{s,k}$ is the Newtonian solvent viscosity, $\mu_{0,k}$ is the total viscosity, α_k is the Giesekus mobility factor and λ_k is the relaxation time of the polymers in $\Omega_k(t)$, $k = 1, 2$, respectively.

The viscoelastic fluid flow in the scaled domain is then described by the dimensionless time-dependent incompressible Navier–Stokes equations

$$\rho \left(\frac{\partial \mathbf{u}}{\partial t} + \mathbf{u} \cdot \nabla \mathbf{u} \right) - \nabla \cdot \mathbb{T}(\mathbf{u}, p, \boldsymbol{\tau}_p) = \frac{\rho \mathbf{e}}{Fr} \quad \text{in } \Omega(t) \times (0, I] \quad (1)$$

$$\nabla \cdot \mathbf{u} = 0 \quad \text{in } \Omega(t) \times (0, I] \quad (2)$$

where (1) is the momentum balance equation and (2) is the mass balance equation. Here, \mathbf{e} is an unit vector in the direction of the

gravitational force. The dimensionless stress tensor $\mathbb{T}(\mathbf{u}, p, \boldsymbol{\tau}_p)$ for an incompressible viscoelastic fluid is given by

$$\mathbb{T}(\mathbf{u}, p, \boldsymbol{\tau}_p) = \frac{2\beta}{\text{Re}} \mathbb{D}(\mathbf{u}) - p\mathbb{I} + \frac{(1-\beta)}{\text{ReWi}} (\boldsymbol{\tau}_p - \mathbb{I}),$$

whereas the velocity deformation tensor $\mathbb{D}(\mathbf{u})$ is given by

$$\mathbb{D}(\mathbf{u}) = \frac{1}{2} (\nabla \mathbf{u} + (\nabla \mathbf{u})^T).$$

Here \mathbb{I} is the identity tensor. The temporal evolution of viscoelastic stresses in the fluid is governed by the Giesekus constitutive equation [5]

$$\overset{\nabla}{\boldsymbol{\tau}}_p + \frac{1}{\text{Wi}} \left[(\boldsymbol{\tau}_p - \mathbb{I}) + \alpha (\boldsymbol{\tau}_p - \mathbb{I})^2 \right] = 0 \quad \text{in } \Omega(t) \times (0, \text{I}), \quad (3)$$

where the upper-convected time derivative of the viscoelastic stress tensor is defined as

$$\overset{\nabla}{\boldsymbol{\tau}}_p = \frac{\partial \boldsymbol{\tau}_p}{\partial t} + (\mathbf{u} \cdot \nabla) \boldsymbol{\tau}_p - \nabla \mathbf{u}^T \cdot \boldsymbol{\tau}_p - \boldsymbol{\tau}_p \cdot \nabla \mathbf{u}. \quad (4)$$

The coupled Navier–Stokes (1), (2) and Giesekus constitutive (3) equations are closed with initial and boundary conditions. At time $t = 0$, we specify the conformation stress tensor $\boldsymbol{\tau}_{p,0}$ and the divergence-free velocity field \mathbf{u}_0 over the entire computational domain Ω_0 , i.e.,

$$\Omega(0) = \Omega_0, \quad \mathbf{u}(\cdot, 0) = \mathbf{u}_0 / U_\infty \text{ in } \Omega_0, \quad \boldsymbol{\tau}_p(\cdot, 0) = \boldsymbol{\tau}_{p,0} \text{ in } \Omega_0.$$

Further, we assume that the boundary $\partial\Omega := \Gamma_D \cup \Gamma_N$ of the computational domain $\Omega(t)$ is fixed in time and we impose the no-slip condition

$$\mathbf{u} = 0 \quad \text{on } \Gamma_D \times (0, \text{I}),$$

and the free-slip condition

$$\boldsymbol{\tau}_N \cdot \mathbb{T}_2(\mathbf{u}, p, \boldsymbol{\tau}_p) \cdot \mathbf{v}_N = 0, \quad \mathbf{u} \cdot \mathbf{v}_N = 0 \quad \text{on } \Gamma_N \times (0, \text{I}),$$

where $\boldsymbol{\tau}_N$ and \mathbf{v}_N are unit tangential and normal vectors respectively on Γ_N . On the interface $\Gamma_F(t)$, we impose the kinematic condition

$$\mathbf{u} \cdot \mathbf{v}_F = \mathbf{w} \cdot \mathbf{v}_F \quad \text{on } \Gamma_F(t) \times (0, \text{I}), \quad (5)$$

and continuity in velocity field

$$[[\mathbf{u}]] = 0 \quad \text{on } \Gamma_F(t) \times (0, \text{I}).$$

Here, \mathbf{w} is the domain velocity, \mathbf{v}_F is an unit normal vector on $\Gamma_F(t)$ and $[[\cdot]]$ denotes the jump of a function at the interface. Further, we impose the force balancing condition

$$[[\mathbb{T}(\mathbf{u}, p, \boldsymbol{\tau}_p)]] \cdot \mathbf{v}_F = \frac{1}{\text{We}} \nabla_{\Gamma_F} \cdot \mathbb{S}_{\Gamma_F} \quad \text{on } \Gamma_F(t) \times (0, \text{I}). \quad (6)$$

Here, the Weber number is defined as

$$\text{We} = \frac{\rho_2 U_\infty^2 L}{\sigma_{ref}}.$$

Further, the surface gradient of a scalar function ψ and the surface divergence of a vector function \mathbf{v} on the interface $\Gamma_F(t)$ are defined by

$$\nabla_{\Gamma_F} \psi = \mathbb{P}_{\mathbf{v}_F} \nabla \psi, \quad \nabla_{\Gamma_F} \cdot \mathbf{v} = \text{tr} \left(\mathbb{P}_{\mathbf{v}_F} \nabla \mathbf{v} \right),$$

where $\mathbb{P}_{\mathbf{v}_F} = \mathbb{I} - \mathbf{v}_F \otimes \mathbf{v}_F$ is the projection onto the tangential plane of $\Gamma_F(t)$. The interface stress tensor \mathbb{S}_{Γ_F} is modeled by

$$\mathbb{S}_{\Gamma_F} = \sigma(C) \mathbb{P}_{\mathbf{v}_F} \quad (7)$$

where C denotes the surfactant concentration on the interface $\Gamma_F(t)$ and $\sigma(C)$ is the interfacial tension coefficient dependent on C . Substituting (7) in the force balancing condition (6), we get

$$\begin{aligned} \nabla_{\Gamma_F} \cdot \mathbb{S}_{\Gamma_F} &= \nabla_{\Gamma_F} \cdot \left(\sigma(C) \mathbb{P}_{\mathbf{v}_F} \right) = \text{tr} \left(\nabla_{\Gamma_F} \left(\sigma(C) \mathbb{P}_{\mathbf{v}_F} \right) \right) \\ &= \mathbb{P}_{\mathbf{v}_F} \nabla_{\Gamma_F} \sigma(C) + \sigma(C) \text{tr} \left(\nabla_{\Gamma_F} \mathbb{P}_{\mathbf{v}_F} \right). \end{aligned} \quad (8)$$

Since the surface gradient is in the tangential plane, we have $\mathbb{P}_{\mathbf{v}_F} \nabla_{\Gamma_F} \sigma(C) = \nabla_{\Gamma_F} \sigma(C)$. Further, one can prove $\text{tr} \left(\nabla_{\Gamma_F} \mathbb{P}_{\mathbf{v}_F} \right) = -\kappa \mathbf{v}_F$, where κ is the sum of principal curvatures, refer [58]. Thus, we have

$$\nabla_{\Gamma_F} \cdot \mathbb{S}_{\Gamma_F} = \nabla_{\Gamma_F} \sigma(C) - \sigma(C) \kappa \mathbf{v}_F. \quad (9)$$

Eq. (9) is the standard form in the literature to include the Marangoni effects. However, we prefer the surface divergence form (8) due to the handling of curvature in the variational form.

The surfactant dependent interfacial tension is given by the Henry linear equation of state, see for example [12,59],

$$\hat{\sigma}(C) = \sigma_{ref} \left(1 + E \left(\frac{C_{ref}}{C_\infty} - C \right) \right) = \sigma_{ref} \sigma(C). \quad (10)$$

Here, σ_{ref} is the reference interfacial tension corresponding to the reference surfactant concentration C_{ref} , E is the Marangoni number given by $E = \text{RTC}_\infty / \sigma_{ref}$, R is the gas constant and T is the absolute temperature.

The surfactant concentration C along the deforming interface $\Gamma_F(t)$ is described by a scalar convection-diffusion equation with a source like term to account for the local changes in the interface area, see for example [10–12]. It reads :

$$\frac{\partial C}{\partial t} + U \cdot \nabla_{\Gamma_F} C - \frac{1}{\text{Pe}} \Delta_{\Gamma_F} C + C \nabla_{\Gamma_F} \cdot \mathbf{u} = 0 \quad \text{in } \Gamma_F(t) \times (0, \text{I}) \quad (11)$$

where

$$\Delta_{\Gamma_F} C = \nabla_{\Gamma_F} \cdot \nabla_{\Gamma_F} C, \quad U = (\mathbf{u} - (\mathbf{u} \cdot \mathbf{v}_F) \mathbf{v}_F), \quad \text{Pe} = \frac{U_\infty L}{D_s}.$$

Here, U is the velocity along the interface, D_s is the interface diffusivity of the surfactant and Pe is the Peclet number. Note that the surfactant concentration C is defined not only on the interface $\Gamma_F(t)$ but also in a neighbourhood of $\Gamma_F(t)$. However, the restriction of $\nabla_{\Gamma_F} C$ on $\Gamma_F(t)$ depends only on values of C on $\Gamma_F(t)$. Surfactant concentration Eq. (11) is closed with an initial condition

$$C(\cdot, 0) = C_0 / C_\infty \quad \text{in } \Gamma_F(0). \quad (12)$$

Note that no boundary condition has to be specified due to the fact that the interface $\Gamma_F(t)$ is a closed surface.

3. Numerical scheme

3.1. Coupled ALE-Lagrangian formulation

The arbitrary Lagrangian–Eulerian (ALE) approach is used to track the interface, see for example [25,45,60,61]. Since, the interface is resolved by the computational mesh in the ALE approach, the spurious velocities if any can be suppressed when the interfacial tension force is incorporated into the numerical scheme accurately [48]. Further, we assume that the topology of the computational domain does not change during the computations. Due to the ALE approach, the time derivative has to be replaced with the time derivative on the reference frame $\hat{\Omega}$ and it results in an addition of convective mesh velocity term in the equations, for more details we refer to [58,60,62]. The ALE form of the Navier–Stokes equations (1), (2) read:

$$\rho \left(\frac{\partial \mathbf{u}}{\partial t} \Big|_{\hat{\Omega}} + ((\mathbf{u} - \mathbf{w}) \cdot \nabla) \mathbf{u} \right) - \nabla \cdot \mathbb{T}(\mathbf{u}, p, \boldsymbol{\tau}_p) = \frac{\rho \mathbf{e}}{\text{Fr}} \quad \text{in } \Omega(t) \times (0, \text{I}), \quad (13)$$

$$\nabla \cdot \mathbf{u} = 0 \quad \text{in } \Omega(t) \times (0, \text{I}). \quad (14)$$

Similarly, the ALE form of Giesekus Eq. (3) read:

$$\begin{aligned} \frac{\partial \boldsymbol{\tau}_p}{\partial t} \Big|_{\hat{\Omega}} + ((\mathbf{u} - \mathbf{w}) \cdot \nabla) \boldsymbol{\tau}_p - \nabla \mathbf{u}^T \cdot \boldsymbol{\tau}_p - \boldsymbol{\tau}_p \cdot \nabla \mathbf{u} \\ + \frac{1}{\text{Wi}} \left[(\boldsymbol{\tau}_p - \mathbb{I}) + \alpha (\boldsymbol{\tau}_p - \mathbb{I})^2 \right] = 0 \quad \text{in } \Omega(t) \times (0, \text{I}). \end{aligned} \quad (15)$$

In computations, we take the previous time-step domain as the reference domain. Since, we move the interface with the fluid velocity in the ALE approach, the surfactant concentration equation is treated in a Lagrangian manner. Hence, the Lagrangian form of Eq. (11) reads:

$$\frac{\partial C}{\partial t} \Big|_{\Gamma_F} - \frac{1}{\text{Pe}} \Delta_{\Gamma_F} C + C \nabla_{\Gamma_F} \cdot \mathbf{u} = 0 \quad \text{in } \Gamma_F(t) \times (0, \text{I}). \quad (16)$$

Note that due to the Lagrangian formulation, the surfactant Eq. (16) does not contain any convective term and hence, we don't need any stabilization scheme while solving it using finite element method.

3.2. Weak formulation

Let $L^2(\Omega(t))$ and $H^1(\Omega(t))$ be the standard Sobolev spaces and (\cdot, \cdot) be the inner product in $L^2(\Omega(t))$ and its vector/tensor-valued versions, respectively. Further, we define the velocity, pressure, viscoelastic stress and surfactant concentration spaces as

$$\begin{aligned} V(\Omega(t)) &:= \{ \mathbf{v} \in H^1(\Omega(t)) : \mathbf{v} \cdot \mathbf{v}_N = 0 \text{ on } \Gamma_N, \mathbf{v} = 0 \text{ on } \Gamma_D \}, \\ Q(\Omega(t)) &:= \left\{ q \in L^2(\Omega(t)) : \int_{\Omega} q \, dx = 0 \right\}, \\ S(\Omega(t)) &:= \{ \boldsymbol{\psi} = [\psi_{ij}], 1 \leq i, j \leq 3 : \psi_{ij} \in H^1(\Omega(t)), \psi_{ij} = \psi_{ji} \}, \\ G(\Gamma_F(t)) &:= \{ \phi \in H^1(\Gamma_F(t)) \}. \end{aligned}$$

To derive the variational formulation of the governing equations, we multiply the ALE form of the momentum (13), mass balance (14) and Giesekus constitutive (15) equations by test functions $\mathbf{v} \in V$, $q \in Q$ and $\boldsymbol{\psi} \in S$, respectively and integrate over the computational domain $\Omega(t)$. After applying integration by parts to the stress tensor term over each sub-domain $\Omega_k(t)$, $k = 1, 2$, and further incorporating all the boundary conditions, the variational form of the governing equations read:

For given $\Omega_0, \mathbf{u}_0/U_\infty, \mathbf{w}, \boldsymbol{\tau}_{p,0}$, find $(\mathbf{u}, p, \boldsymbol{\tau}_p) \in V \times Q \times S$ such that

$$\begin{aligned} \left(\rho \frac{\partial \mathbf{u}}{\partial t}, \mathbf{v} \right)_{\hat{\Omega}} + a(\hat{\mathbf{u}} - \mathbf{w}; \mathbf{u}, \mathbf{v}) - b(p, \mathbf{v}) + c(\boldsymbol{\tau}_p, \mathbf{v}) &= f_1(\mathbf{v}) \\ b(q, \mathbf{u}) &= 0 \\ \left(\frac{\partial \boldsymbol{\tau}_p}{\partial t}, \boldsymbol{\psi} \right)_{\hat{\Omega}} + d(\hat{\mathbf{u}} - \mathbf{w}; \boldsymbol{\tau}_p, \boldsymbol{\psi}) + e(\hat{\boldsymbol{\tau}}_p; \boldsymbol{\tau}_p, \boldsymbol{\psi}) &= f_2(\boldsymbol{\psi}) \end{aligned} \quad (17)$$

for all $(\mathbf{v}, q, \boldsymbol{\psi}) \in V \times Q \times S$, where

$$\begin{aligned} a(\hat{\mathbf{u}} - \mathbf{w}; \mathbf{u}, \mathbf{v}) &= \int_{\Omega(t)} \rho((\hat{\mathbf{u}} - \mathbf{w}) \cdot \nabla) \mathbf{u} \cdot \mathbf{v} \, dx \\ &\quad + \int_{\Omega(t)} \frac{2\beta}{\text{Re}} \mathbb{D}(\mathbf{u}) : \mathbb{D}(\mathbf{v}) \, dx \\ b(q, \mathbf{v}) &= \int_{\Omega(t)} q(\nabla \cdot \mathbf{v}) \, dx \\ c(\boldsymbol{\tau}_p, \mathbf{v}) &= \int_{\Omega(t)} \frac{(1-\beta)}{\text{ReWi}} \boldsymbol{\tau}_p : \mathbb{D}(\mathbf{v}) \, dx \\ f_1(\mathbf{v}) &= \frac{1}{\text{Fr}} \int_{\Omega(t)} \rho(\mathbf{e} \cdot \mathbf{v}) \, dx \\ &\quad - \frac{1}{\text{We}} \int_{\Gamma_F(t)} \mathbb{P}_{\mathbf{v}_F} : \left(\nabla_{\Gamma_{\mathbf{v}_F}} \sigma(C) \mathbf{v} \right) d\gamma_F \\ d(\hat{\mathbf{u}} - \mathbf{w}; \boldsymbol{\tau}_p, \boldsymbol{\psi}) &= \int_{\Omega(t)} (((\hat{\mathbf{u}} - \mathbf{w}) \cdot \nabla) \boldsymbol{\tau}_p) : \boldsymbol{\psi} \, dx \\ &\quad - \int_{\Omega(t)} (\nabla \hat{\mathbf{u}}^T \cdot \boldsymbol{\tau}_p + \boldsymbol{\tau}_p \cdot \nabla \hat{\mathbf{u}}) : \boldsymbol{\psi} \, dx \\ e(\hat{\boldsymbol{\tau}}_p; \boldsymbol{\tau}_p, \boldsymbol{\psi}) &= \int_{\Omega(t)} \frac{\alpha}{\text{Wi}} (\hat{\boldsymbol{\tau}}_p \cdot \boldsymbol{\tau}_p) : \boldsymbol{\psi} \, dx \\ &\quad + \int_{\Omega(t)} \frac{(1-2\alpha)}{\text{Wi}} \boldsymbol{\tau}_p : \boldsymbol{\psi} \, dx \\ f_2(\boldsymbol{\psi}) &= \int_{\Omega(t)} \frac{(1-\alpha)}{\text{Wi}} \mathbb{1} : \boldsymbol{\psi} \, dx. \end{aligned}$$

Further, for ease of notation, we denote

$$\begin{aligned} A(((\hat{\mathbf{u}} - \mathbf{w}), \hat{\boldsymbol{\tau}}_p); (\mathbf{u}, p, \boldsymbol{\tau}_p), (\mathbf{v}, q, \boldsymbol{\psi})) \\ = a(\hat{\mathbf{u}} - \mathbf{w}; \mathbf{u}, \mathbf{v}) - b(p, \mathbf{v}) + c(\boldsymbol{\tau}_p, \mathbf{v}) + b(q, \mathbf{u}) \\ + d(\hat{\mathbf{u}} - \mathbf{w}; \boldsymbol{\tau}_p, \boldsymbol{\psi}) + e(\hat{\boldsymbol{\tau}}_p; \boldsymbol{\tau}_p, \boldsymbol{\psi}). \end{aligned}$$

The interface integral in $f_1(\mathbf{v})$ in the variational form can be rewritten as follows:

$$\begin{aligned} - \frac{1}{\text{We}} \int_{\Gamma_F(t)} \mathbb{P}_{\mathbf{v}_F} : \left(\nabla_{\Gamma_{\mathbf{v}_F}} \sigma(C) \mathbf{v} \right) d\gamma_F \\ = - \frac{1}{\text{We}} \int_{\Gamma_F(t)} \mathbb{P}_{\mathbf{v}_F} : \left[\sigma(C) \left(\nabla_{\Gamma_{\mathbf{v}_F}} \mathbf{v} \right) - E \left(\nabla_{\Gamma_{\mathbf{v}_F}} \sigma(C) \right) \otimes \mathbf{v} \right] d\gamma_F. \end{aligned} \quad (18)$$

The main advantages of the tangential gradient operator technique to handle the curvature are:

- no need to calculate the curvature explicitly
- interfacial tension force can be computed for piecewise smooth surfaces
- only the first derivatives of the basis functions are needed
- interfacial tension force can be treated semi-implicitly giving additional stability.

The variational form of the surfactant concentration Eq. (16) is obtained by multiplying it with a test function $\phi \in G$ and further applying integration by parts for the diffusive term. It reads:

For given $\Gamma_F, \mathbf{u}, C_0/C_\infty$, find $C \in G$ such that

$$\left(\frac{\partial C}{\partial t}, \phi \right)_{\Gamma_F} + \frac{1}{\text{Pe}} \left(\nabla_{\Gamma_{\mathbf{v}_F}} C, \nabla_{\Gamma_{\mathbf{v}_F}} \phi \right) + \left(C \left(\nabla_{\Gamma_{\mathbf{v}_F}} \cdot \mathbf{u} \right), \phi \right) = 0, \quad (19)$$

for all $\phi \in G$. Here, (\cdot, \cdot) denotes the inner product in $L^2(\Gamma_F(t))$ and its vector-valued versions, respectively.

The computational domain is time-dependent and hence, a very fine discretization (both in space and time) is needed to get an accurate solution. This requirement increases the computational cost in 3D. Since the considered domain is rotational symmetric, a 2D geometry with 3D-axisymmetric configuration is used. Thus, we transform the volume and surface integrals in (17), (19) into area and line integrals by using cylindrical coordinates, for more details we refer to [60,62]. It allows us to use two-dimensional finite elements for velocity, pressure and viscoelastic stress, whereas one-dimensional finite element is used for surfactant concentration on the interface. Further, it reduces the computational complexity in the mesh movement as well.

3.3. Spatial discretization

Let $\{\mathcal{T}_h\}$ be a partition of the domain $\Omega(t)$ into an interface resolved triangular mesh using the mesh generator Triangle [63,64]. The diameter of a cell $K \in \mathcal{T}_h$ is denoted by h_K . The mesh parameter h is defined by $h = \max\{h_K \mid K \in \mathcal{T}_h\}$. The discrete form of the domain Ω is given by $\Omega_h := \bigcup_{K \in \mathcal{T}_h} K$, whereas $\hat{\Omega}_h$ denotes the reference domain of Ω_h . Further, let $V_h \subset V$, $Q_h \subset Q$, $S_h \subset S$ and $G_h \subset G$ be the conforming finite element spaces on \mathcal{T}_h . The standard Galerkin approach to solve the viscoelastic constitutive equation leads to unphysical oscillations in the numerical solution when the constitutive equation is highly advection dominated at high Weissenberg numbers. Further, the choice of finite element spaces for the velocity, pressure and viscoelastic stress is subject to two discrete inf-sup conditions, refer [57]. Finite elements that satisfy both discrete inf-sup conditions simultaneously are rare. A possible remedy to the above two shortcomings of the standard Galerkin approach for the coupled problem (17) is to use a stabilized formulation. In this work, we use the Local Projection Stabilization (LPS) method. LPS was originally proposed for the Stokes problem by Becker and Braack [65], and later it has been extended for transport [66] and Oseen [67] problems. Recently, LPS technique has been used by Venkatesan and Ganesan [45,57,62] for the simulation of viscoelastic fluid flows. There are two variants of LPS implementation, namely one-level and two-level approach. In this work, we use the one-level LPS variant [57,68–70], which is based on enrichment of approximation spaces and it allows us to perform the computations on a single mesh as the approximation and the projection spaces are defined on the same mesh.

Let Y_h denote the approximation space and D_h be the discontinuous projection space defined on \mathcal{T}_h . Let $D_h(K) := \{d_h|_K : d_h \in D_h\}$ and π_K :

$Y_h(K) \rightarrow D_h(K)$ be the local L^2 -projection into $D_h(K)$. Further, we define the global projection $\pi_h: Y_h \rightarrow D_h$ by $(\pi_h \gamma)|_K := \pi_K(\gamma|_K)$. The fluctuation operator $\kappa_h: Y_h \rightarrow Y_h$ is given by $\kappa_h := id - \pi_h$, where id is the identity mapping. The local projection stabilized finite element approximation of the variational problem (17) reads:

For given $\Omega_0, \mathbf{u}_0/U_\infty, \mathbf{w}_h$ and $\tau_{p,0}$, find $(\mathbf{u}_h, p_h, \tau_{p,h}) \in V_h \times Q_h \times S_h$ such that

$$\left(\rho \frac{\partial \mathbf{u}_h}{\partial t}, \mathbf{v}_h\right)_{\hat{\Omega}_h} + \left(\frac{\partial \tau_{p,h}}{\partial t}, \Psi_h\right)_{\hat{\Omega}_h} + S_1(\mathbf{u}_h, \mathbf{v}_h) + S_2(\tau_{p,h}, \Psi_h) + A((\hat{\mathbf{u}}_h - \mathbf{w}_h), \hat{\tau}_{p,h}; (\mathbf{u}_h, p_h, \tau_{p,h}), (\mathbf{v}_h, q_h, \Psi_h)) = f_1(\mathbf{v}_h) + f_2(\Psi_h) \quad (20)$$

for all $(\mathbf{v}_h, q_h, \Psi_h) \in V_h \times Q_h \times S_h$, where

$$S_1(\mathbf{u}_h, \mathbf{v}_h) = \sum_{K \in \mathcal{T}_h} \varsigma_1 \langle \kappa_h \mathbb{D}(\mathbf{u}_h), \kappa_h \mathbb{D}(\mathbf{v}_h) \rangle_K$$

$$S_2(\tau_{p,h}, \Psi_h) = \sum_{K \in \mathcal{T}_h} \varsigma_2 \langle \kappa_h (\nabla \cdot \tau_{p,h}), \kappa_h (\nabla \cdot \Psi_h) \rangle_K + \sum_{K \in \mathcal{T}_h} \varsigma_3 \langle \kappa_h \nabla \tau_{p,h}, \kappa_h \nabla \Psi_h \rangle_K.$$

Here, $\varsigma_1 = (1 - \beta)c_1 h_K, \varsigma_2 = c_2 h_K, \varsigma_3 = c_3 h_K$, with c_1, c_2 and c_3 being user-chosen constants. The numerical scheme allows us to use inf-sup stable finite elements for the velocity and pressure spaces, and equal order interpolation spaces for the velocity and viscoelastic stress. In particular, we use the following triplet $(V_h, Q_h, S_h) = (P_2^{bubble}, P_1^{disc}, P_2^{bubble})$. By approximating the pressure with discontinuous elements, we shall suppress the spurious velocities [48] during computations. Moreover, we achieve better mass conservation, since the first integral moments of the divergence of velocity field vanishes element-wise with discontinuous pressure approximation. For more details on LPS for viscoelastic fluid flows we refer to [45,57,62].

The standard Galerkin finite element approximation of the variational form of surfactant concentration Eq. (19) reads:

For given $\Gamma_F, \mathbf{u}_h, C_0/C_\infty$, find $C_h \in G_h$ such that

$$\left(\frac{\partial C_h}{\partial t}, \phi_h\right)_{\hat{\Gamma}_F} + \frac{1}{\text{Pe}} (\nabla_{\Gamma_F} C_h, \nabla_{\Gamma_F} \phi_h) + (C_h (\nabla_{\Gamma_F} \cdot \mathbf{u}_h), \phi_h) = 0, \quad (21)$$

for all $\phi_h \in G_h$. We use quadratic finite elements for the surfactant concentration.

3.4. Time discretization and linearization

Let $0 = t^0 < t^1 < \dots < t^N = I$ be a decomposition of the time interval $[0, I]$, and $\delta t = t^{n+1} - t^n, n = 0, \dots, N - 1$, be a uniform time step. We use the first-order implicit Euler method for the time discretization of the coupled system (20), (21) in the time interval (t^n, t^{n+1}) . Investigations in [71] show that an implicit handling of the curvature term is needed for unconditional stability. However, its too complicated because we need in advance the interface Γ_F^{n+1} , which is unknown. Thus, as in [72], we use a semi-implicit approximation of the curvature term (first term in (18))

$$-\frac{1}{\text{We}} \int_{\Gamma_F^{n+1}} \sigma(C) \mathbb{P}_{\mathbf{v}_F^{n+1}} : (\nabla_{\Gamma_F} \mathbf{v}_h) d\gamma_F$$

$$= -\frac{1}{\text{We}} \int_{\Gamma_F^n} \sigma(C) \left[\mathbb{P}_{\mathbf{v}_F^n} + \delta t \nabla_{\Gamma_F} \mathbf{u}_h^{n+1} \right] : (\nabla_{\Gamma_F} \mathbf{v}_h) d\gamma_F.$$

Consequently, the curvature term is splitted into an explicit term on the right hand side of the weak formulation

$$-\frac{1}{\text{We}} \int_{\Gamma_F^n} \sigma(C) \mathbb{P}_{\mathbf{v}_F^n} : (\nabla_{\Gamma_F} \mathbf{v}_h) d\gamma_F$$

and an implicit term on the left hand side

$$\frac{\delta t}{\text{We}} \int_{\Gamma_F^n} \sigma(C) (\nabla_{\Gamma_F} \mathbf{u}_h^{n+1}) : (\nabla_{\Gamma_F} \mathbf{v}_h) d\gamma_F,$$

which is symmetric and positive semi-definite and thus, it improves the stability of the discrete system compared to a fully explicit approach.

Let $\mathbf{u}_{h,0}^{n+1} = \mathbf{u}_h^n, \tau_{p,h,0}^{n+1} = \tau_{p,h}^n$ and $\mathbf{w}_{h,0}^{n+1} = \mathbf{w}_h^n$. We adopt the following linearization strategy for the nonlinear terms in (20):

$$a(\mathbf{u}_h^{n+1} - \mathbf{w}_h^{n+1}; \mathbf{u}_h^{n+1}, \mathbf{v}_h) \approx a(\mathbf{u}_{h,m-1}^{n+1} - \mathbf{w}_{h,m-1}^{n+1}; \mathbf{u}_{h,m}^{n+1}, \mathbf{v}_h)$$

$$d(\mathbf{u}_h^{n+1} - \mathbf{w}_h^{n+1}; \tau_{p,h}^{n+1}, \Psi_h) \approx d(\mathbf{u}_{h,m-1}^{n+1} - \mathbf{w}_{h,m-1}^{n+1}; \tau_{p,h,m}^{n+1}, \Psi_h) + d(\mathbf{u}_{h,m}^{n+1}, \tau_{p,h,m-1}^{n+1}, \Psi_h) - d(\mathbf{u}_{h,m-1}^{n+1}; \tau_{p,h,m-1}^{n+1}, \Psi_h)$$

$$e(\tau_{p,h}^{n+1}; \tau_{p,h}^{n+1}, \Psi_h) \approx e(\tau_{p,h,m-1}^{n+1}; \tau_{p,h,m}^{n+1}, \Psi_h),$$

where, $m = 1, 2, \dots, M$, with M being the maximum allowed number of nonlinear iterations. In each fixed point iteration, we solve the linear elasticity problem (refer [45]) to calculate the unknown mesh velocity $\mathbf{w}_{h,m-1}^{n+1}$ ‘virtually’ without moving the mesh. In all computations, the iterations are continued until the residual of the monolithic system becomes less than the threshold value of 10^{-7} . In general this condition is fulfilled within 2 to 3 iteration steps. After stopping the fixed point iteration, we solve the surfactant concentration equation before moving the mesh to a new position. The linearized system of algebraic equations are solved using the Multifrontal Massively Parallel Sparse (MUMPS) direct solver [73,74]. The proposed numerical scheme for the simulation of viscoelastic two-phase flows with insoluble surfactants is implemented in our in-house finite element code ParMoon [75].

The limits of the proposed numerical scheme are as follows: the developed scheme is for axisymmetric flows. The scheme shall not be applicable for asymmetric flows since full 3D simulations need to be performed. Further, we have assumed that the flow is isothermal and the material properties like density, viscosity and relaxation time of polymers remain constant throughout the computations. However, in most practical applications it may not be the case. Further, we assumed that there is no topological change during the computations, that is, computations cannot be continued with the proposed scheme when a single drop splits into two or more droplets.

4. Numerical results

In this section, we present a detailed numerical investigation of 3D-axisymmetric buoyancy driven viscoelastic two-phase flows with insoluble surfactants on the interface. We first perform a grid independence test for a 3D-axisymmetric viscoelastic drop rising in a Newtonian fluid column. Further, to validate the numerical scheme, computations are performed with 2D planar configuration for a buoyancy driven Newtonian bubble rising in a Newtonian fluid column and compared with the benchmark results [61]. In addition, we compare the computational results of 2D planar Newtonian drop rising in an Giesekus fluid column with the results of Vahabi and Kamkari [76]. Next, we present the computational results for a buoyancy driven viscoelastic drop rising in a Newtonian fluid column with insoluble surfactants on the interface. Moreover, the effects of Marangoni number (E), initial surfactant concentration (C_0) and Peclet number (Pe) on the rising drop dynamics are examined. In addition, we investigate the flow dynamics of a Newtonian drop rising in a viscoelastic fluid column with insoluble surfactants on the interface.

The computational domain is triangulated into an interface resolved mesh using the mesh generator Triangle [63,64] based on constrained Delaunay triangulation. The constraints are the number of vertices on each boundary and the maximum area of each cell. We limit the maximum area of each cell in the domain to 0.001 during the triangulation (initially and as well as during the remeshing). In computations, the number of cells and the number of degrees of freedom might change during the remeshing. The finite element spaces used in computations for the velocity, pressure, viscoelastic stress and surfactant

concentration on the interface are P_2^{bubble} , P_1^{disc} , P_2^{bubble} and P_2 respectively. Further, the stabilization constants used in computations are $c_1 = 0.005$, $c_2 = 0.005$ and $c_3 = 0.005$.

The flow dynamics of the rising drop is analyzed using the following parameters: drop shape, diameter of the drop at the axis of symmetry ($D|_{r=0}$), sphericity, kinetic energy, elastic energy, center of mass (z coordinate), rise velocity and surfactant concentration on the interface. Let $|\Omega_1(t)| := 2\pi \int_{\Omega_1(t)} r dr dz$ be the volume of the drop. The kinetic and elastic energies of the drop are calculated as follows:

$$E_{kinetic} = \frac{2\pi}{|\Omega_1(t)|} \int_{\Omega_1(t)} (\mathbf{u} \cdot \mathbf{u}) r dr dz,$$

$$E_{elastic} = \frac{2\pi}{|\Omega_1(t)|} \int_{\Omega_1(t)} tr(\boldsymbol{\tau}_p) r dr dz,$$

where tr denotes the trace of the tensor. Further, the rise velocity and center of mass (z coordinate) of the drop are computed as:

$$\text{Rise velocity} = \frac{2\pi}{|\Omega_1(t)|} \int_{\Omega_1(t)} u_z r dr dz,$$

$$\text{Center of mass} = \frac{2\pi}{|\Omega_1(t)|} \int_{\Omega_1(t)} z r dr dz.$$

The sphericity of the drop is given by

$$\text{Sphericity} = \frac{\text{surface area of the volume-equivalent sphere}}{\text{surface area of the drop}} = \frac{A_e}{A}.$$

The surface area of volume-equivalent sphere and surface area of the drop are calculated as follows:

$$A_e = 4\pi \left(\frac{3}{4\pi} |\Omega_1(t)| \right)^{2/3}, \quad A = 2\pi \int_{\partial\Omega_1(t)} r dl.$$

For a perfectly spherical drop, the sphericity will be one and for any other deformed drop it will be less than one. It is a good quantitative measure of the drop deformation. Further, to measure the accuracy of the numerical scheme, we compute the relative volume loss and

Table 1

Grid independence test: characteristics of triangular meshes.

Mesh	DOFs on Γ_F	h_0	Cells	Total DOFs
L0	50	0.03139526	2,000	56,776
L1	100	0.01570538	2,267	64,337
L2	200	0.007853659	2,912	82,522
L3	400	0.003926950	4,152	117,493
L4	500	0.003141572	4,641	131,259

surfactant mass loss as follows:

$$\text{volume loss(\%)} = \frac{|\Omega_1(t)| - |\Omega_1(0)|}{|\Omega_1(0)|} \times 100,$$

$$\text{surfactant mass loss(\%)} = \frac{\int_{\Gamma_{F(t)}} Cr dr dz - \int_{\Gamma_{F(0)}} Cr dr dz}{\int_{\Gamma_{F(0)}} Cr dr dz} \times 100.$$

In all our computations, we found that the relative volume loss is always less than 0.075% and the surfactant mass loss is less than 0.05%.

4.1. Grid independence test

In this section, we perform a grid independence test for the proposed local projection stabilized numerical scheme for computations of 3D-axisymmetric viscoelastic two-phase flows with insoluble surfactants. We consider a viscoelastic drop rising in a Newtonian fluid column with the following dimensionless flow parameters: $Re_2 = 10$, $Fr = 1$, $We = 400$, $Wi_1 = 5$, $\epsilon = 2$, $\rho_1/\rho_2 = 0.1$, $\beta_1 = 0.75$, $\beta_2 = 1.0$, $\alpha_1 = 0.1$, $Pe = 50$, $C_0 = 0.5$, $C_\infty = 1$, $C_{ref} = 0.5$, $E = 1$, $D = 0.5$ and $h_c = 2.5$. To perform a grid independence test, we vary the number of degrees of freedom (DOFs) on the interface. Five different meshes are used in this study and the characteristics of these meshes at time $t = 0$ are tabulated in Table 1. Further, the time step length is set as $\delta t = 0.001$ and the computations are performed till $I = 20$.

Fig. 2 depicts the convergence behaviour of the drop shape at $t = 20$, elastic energy in the drop and center of mass of the rising drop for all

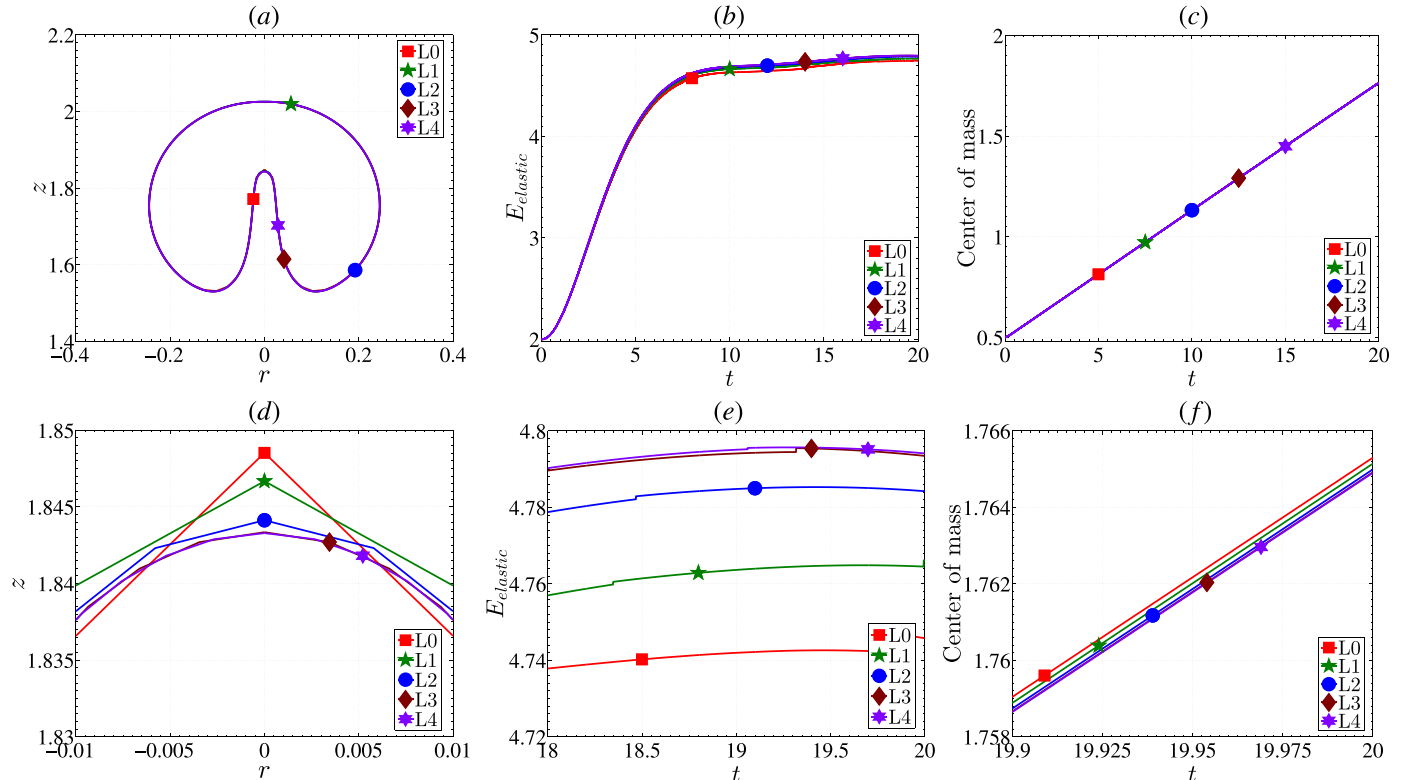


Fig. 2. Grid independence test: (a) drop shape at $t = 20$, (b) elastic energy in the drop, (c) center of mass of the drop, (d), (e) and (f) are the magnified view of the plots (a), (b) and (c) respectively using five different meshes.

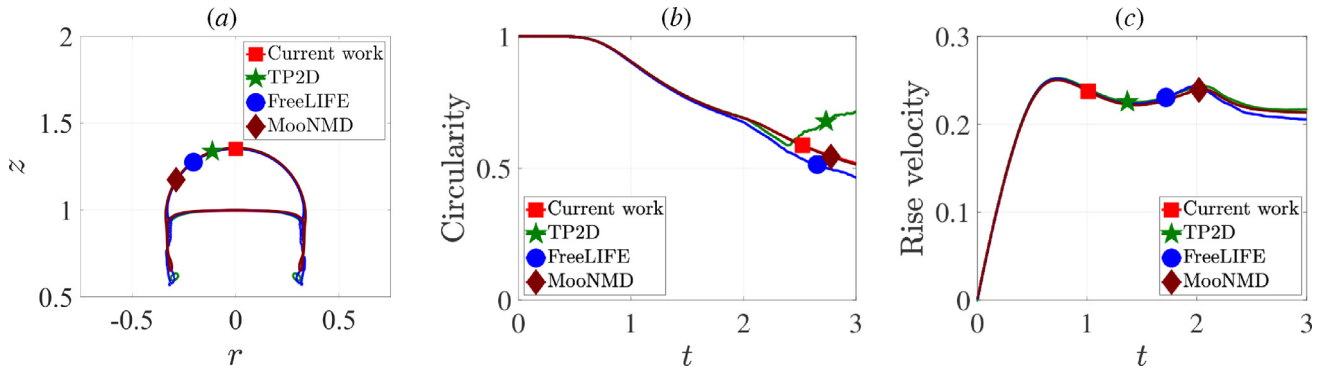


Fig. 3. Validation of numerical scheme: (a) bubble shape at $t = 3$ s, (b) circularity and (c) rise velocity of a Newtonian bubble rising in a Newtonian fluid column compared with the numerical results from the three participating groups in the benchmark paper [61], namely TP2D, FreeLIFE and MooNMD.

the five mesh levels. The drop shape at $t = 20$ obtained using all the five mesh levels are almost similar. However, a close-up look near the tail end of the drop at the axis of symmetry, see Fig. 2(d), clearly shows that the results obtained with L3 and L4 meshes are almost identical. Similar convergence behaviour is observed in the elastic energy in the drop and the center of mass of the drop, see Fig. 2(e) and (f) respectively. In order to have a fine balance between the computational cost and the accuracy, all numerical results in the following section is obtained with the mesh L3.

4.2. Validation

In order to validate the numerical scheme, we first consider a 2D planar Newtonian bubble rising in a Newtonian fluid column as described in the benchmark paper of Hysing et al. [61]. The benchmark parameters are as follows: $\rho_1 = 1$, $\rho_2 = 1000$, $\mu_{0,1} = 0.1$, $\mu_{0,2} = 10$, $g = 0.98$, $\sigma = 1.96$, $D = 0.5$ and $h_c = 2.0$ (refer test case-2 in Table 1 of [61]). Using the characteristic length $L = 1$ and characteristic velocity $U_\infty = \sqrt{Lg}$, we get the following dimensionless quantities $Re_2 = 99$, $Fr = 1$, $We = 500$, $\rho_1/\rho_2 = 0.001$, $\epsilon = 100$, $\beta_1 = 1$ and $\beta_2 = 1$. We use 800 degrees of freedom on the interface and the time step length is set as $\delta t = 0.0005$. Fig. 3 depicts the bubble shape at $t = 3$ s, circularity and rise velocity and compared with the results of the three participating groups in the benchmark paper [61], namely TP2D, FreeLIFE and MooNMD. TP2D and FreeLIFE are finite element based codes and level set method is used to capture the interface. Further, in MooNMD iso-parametric finite elements have been used along with the arbitrary Lagrangian-Eulerian technique to capture the interface. Moreover, TP2D and FreeLIFE can handle break-up of the bubble, while no criteria for the break up of the bubble has been implemented in MooNMD. For more details about the three benchmark codes, we refer to [61]. Since, our work is based on the coupled ALE-Lagrangian approach, we expect our results to be close to the results of MooNMD which also uses ALE approach.

In Fig. 3(a), we can observe that all codes predict a similar shape for the main bulk of the bubble, whereas there is no agreement in our bubble shape to those of TP2D and FreeLIFE with respect to the thin filamentary regions. However, our bubble shape coincides with the earlier results in MooNMD even in the thin filamentary regions despite a different mesh used in this present study. From Fig. 3(b) and (c), we observe excellent agreement in circularity of the bubble and rise velocity curves with all the benchmark results till $t = 1.75$ – 2.0 , after which there are significant differences and this is due to the thin filamentary regions. Beyond $t = 2.0$, there is no real agreement between the three groups in the benchmark paper [61]. Further, in order to qualitatively compare our numerical solutions with the results of the three groups in the benchmark paper [61], the minimum circularity, maximum rise velocity with corresponding incidence times and the final position of the center of mass are tabulated in Table 2. We

can observe that our results are quite similar to the results of TP2D except for minimum circularity and its corresponding time, in addition to an excellent agreement with MooNMD results in the benchmark paper [61].

The next test case is a 2D planar Newtonian drop rising in a Giesekus fluid column as described by Vahabi and Kamkari [76]. The flow parameters are defined as: $\rho_1 = 100$, $\rho_2 = 1000$, $\mu_{0,1} = 0.1025$, $\mu_{0,2} = 1.025$, $g = 9.8$, $\sigma = 0.01$, $\lambda_2 = 0.2$ and $\alpha_2 = 0.5$. Using the characteristic length $L = 0.01$ and characteristic velocity $U_\infty = \sqrt{Lg}$, we get the following dimensionless quantities $Re_2 = 3.054$, $Fr = 1$, $We = 98$, $Wi_2 = 6.26$, $\rho_1/\rho_2 = 0.1$, $\epsilon = 10$, $\alpha_2 = 0.5$, $\beta_1 = 1$ and $\beta_2 = 0.286$. Fig. 4 depicts the drop shape at 0.16 seconds and compared with the results of Vahabi and Kamkari [76]. As it is observed, the results are almost the same revealing that the developed code is well capable to predict the behavior of a rising drop in a fluid column with viscoelastic effects modeled by the Giesekus constitutive equation.

Table 2

Newtonian bubble rising in a Newtonian fluid column: comparison of our results with the numerical solutions from the three participating groups in the benchmark paper [61], namely TP2D, FreeLIFE and MooNMD.

Reference	Current work	TP2D	FreeLIFE	MooNMD
min (Circularity)	0.5195	0.5869	0.4647	0.5144
$t _{\min}$ (Circularity)	3.0000	2.4004	3.0000	3.0000
max 1 (Rise velocity)	0.2503	0.2524	0.2514	0.2502
$t _{\max 1}$ (Rise velocity)	0.7328	0.7332	0.7281	0.7317
max 2 (Rise velocity)	0.2390	0.2434	0.2440	0.2393
$t _{\max 2}$ (Rise velocity)	2.0685	2.0705	1.9844	2.0600
Center of mass at $t = 3.0$	1.1373	1.1380	1.1249	1.1376

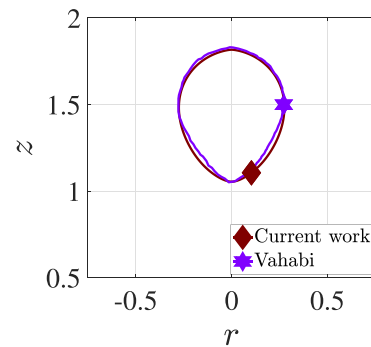


Fig. 4. Validation of numerical scheme: drop shape at $t = 0.16$ s of a Newtonian drop rising in a Giesekus fluid column compared with the results of Vahabi and Kamkari [76].

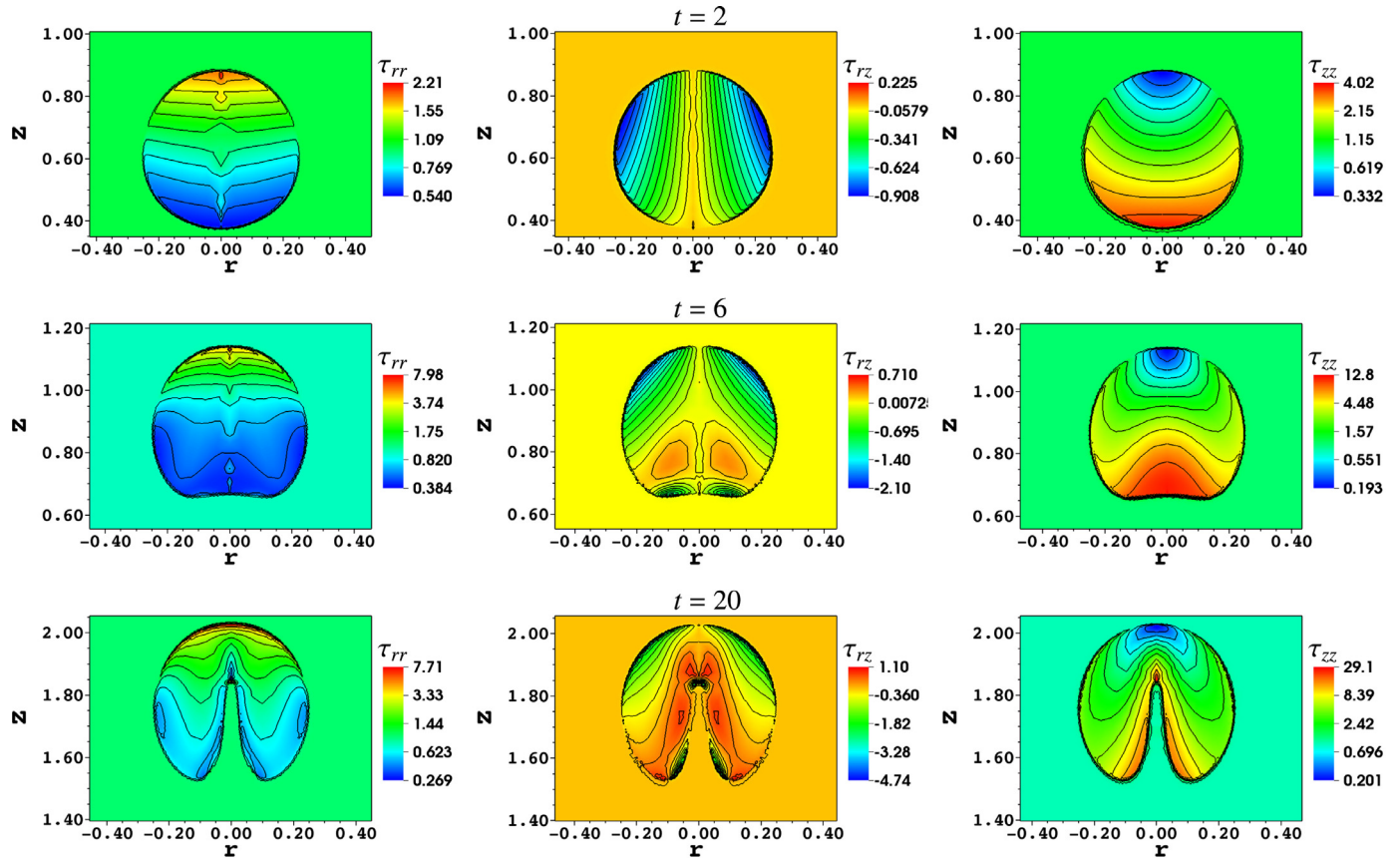


Fig. 5. Viscoelastic conformation stress profiles for a viscoelastic drop rising in a Newtonian fluid column with insoluble surfactants on the interface with flow parameters $Re_2 = 10$, $Fr = 1$, $We = 400$, $Wi_1 = 5$, $\rho_1/\rho_2 = 0.1$, $\epsilon = 2$, $\beta_1 = 0.75$, $\beta_2 = 1.0$, $\alpha_1 = 0.1$, $Pe = 50$, $C_0 = 0.5$, $C_\infty = 1$, $C_{ref} = 0.5$, $E = 1$, $D = 0.5$ and $h_c = 2.5$ at dimensionless times $t = 2, 6$ and 20 .

4.3. Viscoelastic drop rise in a Newtonian fluid column with insoluble surfactants

In this section, we consider a buoyancy driven 3D-axisymmetric viscoelastic drop rising in a Newtonian fluid column with insoluble surfactants on the interface. To systematically examine the effects of various flow parameters, we designate a base case which is defined as: $Re_2 = 10$, $Fr = 1$, $We = 400$, $Wi_1 = 5$, $\epsilon = 2$, $\rho_1/\rho_2 = 0.1$, $\beta_1 = 0.75$, $\beta_2 = 1.0$, $\alpha_1 = 0.1$, $Pe = 50$, $C_0 = 0.5$, $C_\infty = 1$, $C_{ref} = 0.5$, $E = 1$, $D = 0.5$ and $h_c = 2.5$. Fig. 5 presents the viscoelastic stress profiles for the base case flow parameters at dimensionless time instances $t = 2, 6$ and 20 . Further, the surfactant concentration profile along the interface at different time instances has been presented in Fig. 6.

At time $t = 0$, the drop is of a spherical shape with initial velocities of the drop and the bulk fluid column assumed to be zero and the viscoelastic conformation stress tensor is set as $\tau_{p,0} = \mathbb{I}$. The difference in densities of the drop and the bulk fluid column generates a buoyancy force that accelerates the drop in the vertical upward direction. The motion of the rising drop depends on the magnitude of viscous stress, viscoelastic stress and the Marangoni effects due to the presence of insoluble surfactants on the interface. The shape of the drop depends on the deforming stresses and the interfacial tension force. If the deforming stresses at the interface are sufficiently smaller than the interfacial tension force, the drop shape remains approximately spherical. However, when these deforming stresses are significant the interface deforms and the drop shape changes depending on the properties of the bulk fluid: it deforms to an oblate shape in inertia-dominated flows and to a prolate shape with or without an indentation at the trailing end in flows in which viscoelasticity is important. Further, in flows with surfactants the interfacial tension becomes low when the surfactant concentration

increases and vice-versa. The presence of the interfacial tension gradient along the interface causes the liquid to move away from the low interfacial tension regime.

The initial motion of the drop is dominated by viscous stresses as the viscoelastic stresses take some time to build up. Further, along the interface, the interfacial tension force dominates compared to the viscous and viscoelastic stresses. Hence, the shape of the drop is more spherical at $t = 2$. In Fig. 6, we can observe that initially the surfactant concentration is uniform along the interface with a value $C_0 = 0.5$. As the drop rises due to buoyancy, the concentration of the surfactant increases near the

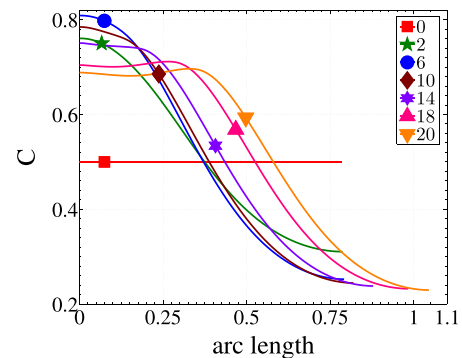


Fig. 6. Surfactant concentration profile along the interface for a viscoelastic drop rising in a Newtonian fluid column at time instances $t = 0, 2, 6, 10, 14, 18$ and 20 for the base case with flow parameters $Re_2 = 10$, $Fr = 1$, $We = 400$, $Wi_1 = 5$, $\rho_1/\rho_2 = 0.1$, $\epsilon = 2$, $\beta_1 = 0.75$, $\beta_2 = 1.0$, $\alpha_1 = 0.1$, $Pe = 50$, $C_0 = 0.5$, $C_\infty = 1$, $C_{ref} = 0.5$, $E = 1$, $D = 0.5$ and $h_c = 2.5$.

rear end of the drop while it decreases at the top end of the drop compared to the initial concentration. Hence, at the rear end the drop becomes more easily deformable due to lower interfacial tension, whereas at the top end it becomes difficult to deform due to higher interfacial tension.

At $t = 6$, we can observe that the drop at the rear end starts to deform and it attains a cylindrical shape with a dimpled trailing end. By this time, the viscous and viscoelastic stresses start to overcome the interfacial tension at the rear end of the drop. This is aided by the reduction in the interfacial tension at the trailing end due to surfactant migration. In Fig. 5, we can observe that the maximum values of viscoelastic stress component τ_{rr} are concentrated in the top end of the drop, while τ_{zz} is built up more near the tail end of the drop. The polymers inside the drop is stretched along the flow direction. Since the local flow direction is normal to the interface at the rear stagnation point, the viscoelastic stress component τ_{zz} reaches its maximum value at the tail end of the drop and pulls the interface inward. Since, the maximum values of τ_{rr} and minimum values of τ_{zz} occur at the top end of the drop, the upstream axial flow experiences a strong turn tangential to the drop surface so that the polymers are greatly extended in the radial directions. Thus, the drop doesn't experience noticeable deformation at its front end.

With progress in time, the magnitude of viscoelastic stresses increase, and the drop continues to deform at the trailing end. In particular, the drop at the tail end gets pulled up even more. The surfactant concentration increases at the tail end till $t = 6$, after which it decreases. This is due to the fact near the tail end of the drop, the interfacial area increases with time due to large deformation at the tail end and hence, the surfactant is spread over more interfacial area and thus, it gets spread over area rather than just at the tip. The simulations were stopped at $t = 20$, as beyond that the drop shall start to split and the assumption of

no topological change in the computational domain shall fail when the drop splits.

In all two-phase flow computations involving viscoelasticity, low density and viscosity ratios have been used due to the challenge in convergence. At high density and viscosity ratios, there would be very high gradients in the viscoelastic stress which could be handled by choosing the stabilization parameter adaptively and it needs further investigation.

Next, we perform a parametric study to examine the effects of Marangoni number, initial surfactant concentration and Peclet number on the rising viscoelastic drop dynamics in a Newtonian fluid column. For the effects of other parameters like the viscosity ratio, Newtonian solvent ratio, Giesekus mobility factor and Weber number in the absence of insoluble surfactants, we refer to [45].

4.3.1. Influence of Marangoni number

In this section, we study the influence of Marangoni number on the rising viscoelastic drop dynamics in a Newtonian fluid column with insoluble surfactants on the interface. We consider the base case flow parameters and vary only the Marangoni number. The following five different Marangoni numbers are used in this study: (i) $E = 0$, (ii) $E = 0.5$, (iii) $E = 1.0$, (iv) $E = 1.5$ and (v) $E = 2.0$. The case $E = 0$ represents the clean case, i.e. no surfactants on the interface. Fig. 7 presents the drop shape at $t = 20$, diameter of the drop at $r = 0$, sphericity, elastic energy, rise velocity and kinetic energy in the drop for different Marangoni numbers.

In the presence of surfactants on the interface, the interfacial tension becomes low when the surfactant concentration increases and vice-versa. Fig. 8 presents the surfactant concentration profile along the interface at different time instances for the cases $E = 0.5$ and $E = 2.0$.

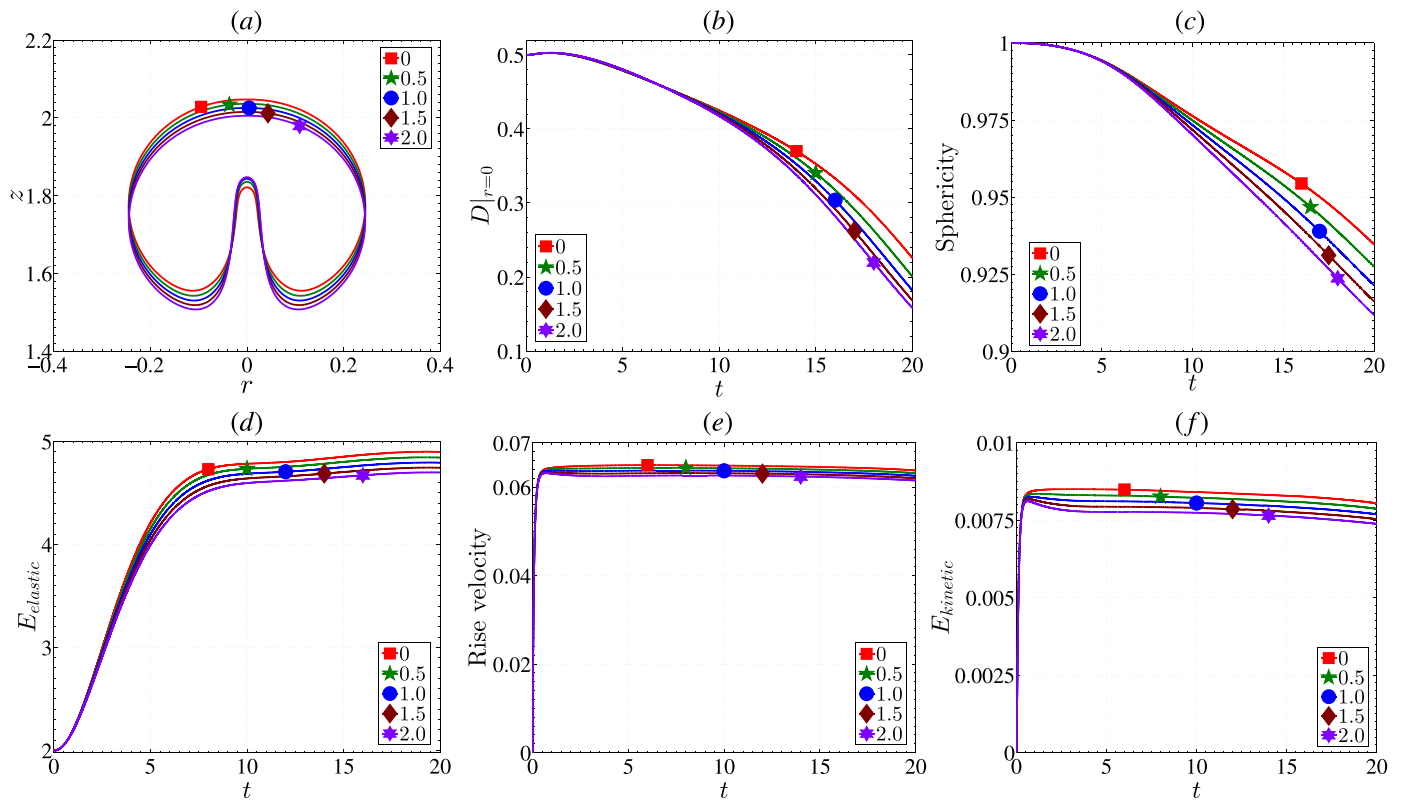


Fig. 7. Influence of Marangoni number for a viscoelastic drop rising in a Newtonian fluid column: (a) drop shape at $t = 20$, (b) diameter of the drop at $r = 0$, (c) sphericity, (d) elastic energy, (e) rise velocity and (f) kinetic energy for different Marangoni numbers (i) $E = 0$, (ii) $E = 0.5$, (iii) $E = 1.0$, (iv) $E = 1.5$ and (v) $E = 2.0$ with $Re_2 = 10$, $Fr = 1$, $We = 400$, $Wi_1 = 5$, $\rho_1/\rho_2 = 0.1$, $\epsilon = 2$, $\beta_1 = 0.75$, $\beta_2 = 1.0$, $\alpha_1 = 0.1$, $C_0 = 0.5$, $C_\infty = 1$, $C_{ref} = 0.5$, $Pe = 50$, $D = 0.5$ and $h_c = 2.5$.

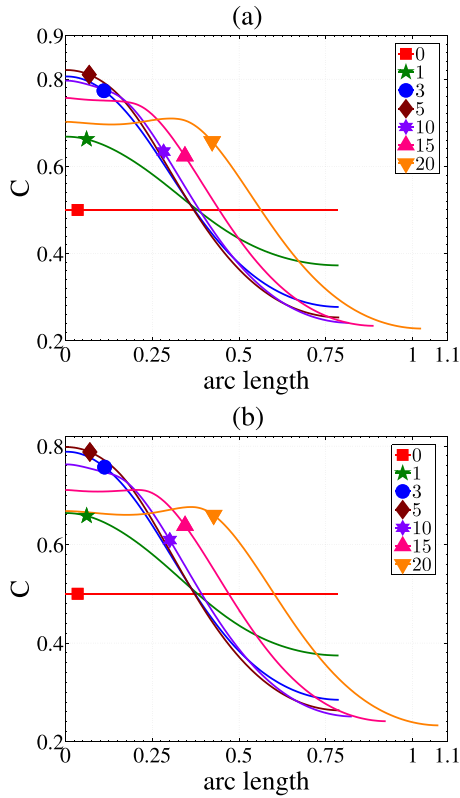


Fig. 8. Surfactant concentration profile along the interface for a viscoelastic drop rising in a Newtonian fluid column at different time instances for the cases (a) $E = 0.5$ and (b) $E = 2.0$.

From Fig. 8, the effect of surfactants on the rising drop dynamics can be understood by observing how the surfactant concentration evolves over time along the interface. Initially, we start with an uniform surfactant concentration $C_0 = 0.5$. It is seen that the surfactant concentration at the trailing end quickly increases to a maximum, and then slowly decreases. The local maxima moves away from central tip (arc length = 0) as the drop deforms. We can also see that the arc length of the drop increases with time (as it deforms and becomes less spherical), which contributes to the reduction of average surfactant concentration.

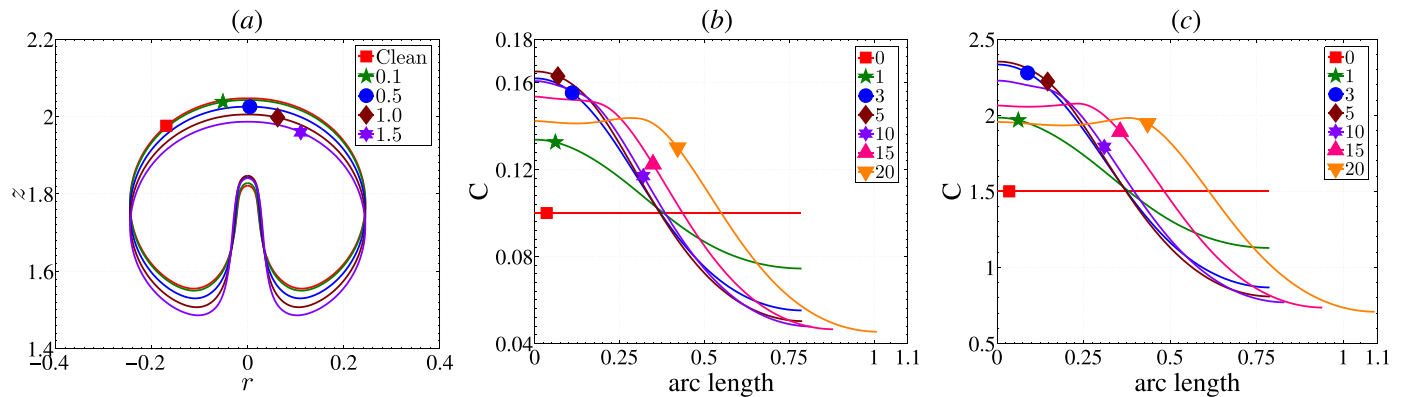


Fig. 9. Influence of initial surfactant concentration for a viscoelastic drop rising in a Newtonian fluid column: (a) drop shape at $t = 20$ for different initial surfactant concentrations (i) $C_0 = 0.1$, (ii) $C_0 = 0.5$, (iii) $C_0 = 1.0$ and (iv) $C_0 = 1.5$, surfactant concentration profile along the interface at different time instances for the cases (b) $C_0 = 0.1$ and (c) $C_0 = 1.5$ with flow parameters $Re_2 = 10$, $Fr = 1$, $We = 400$, $Wi_1 = 5$, $\rho_1/\rho_2 = 0.1$, $\epsilon = 2$, $\beta_1 = 0.75$, $\beta_2 = 1.0$, $\alpha_1 = 0.1$, $E = 1$, $Pe = 50$, $D = 0.5$ and $h_c = 2.5$.

Till $t = 5$, the surfactant concentration increases at the tail end of the drop and decreases at the top end compared to the initial concentration. Due to the non-uniform distribution of surfactant concentration on the interface, there will be an interfacial tension gradient. The presence of the interfacial tension gradient causes the liquid to move away from the low interfacial tension regime. Hence, near the tail end of the drop, it will be pulled up more compared to the clean case and the same is observed in the drop shape at $t = 20$, refer Fig. 7(a). Marangoni number is nothing but the rate of increase/decrease of the interfacial tension coefficient. Hence, with increase in the Marangoni number, the interfacial tension coefficient either increases more rapidly or decreases more rapidly depending on the surfactant concentration at a particular point on the interface. Thus, the drop shape at $t = 20$ is pulled up more as the Marangoni number is increased. Due to this phenomenon, the temporal evolution of the diameter of the drop at $r = 0$ decreases more with increase in the Marangoni number, see Fig. 7(b). Similar behaviour is observed in the sphericity curve as well, see Fig. 7(c), as sphericity is a measure of the deformation of the drop relative to the initial spherical shape. Further, the elastic energy in the drop increases with time as the viscoelastic stresses are developed based on the gradient of the fluid velocity. However, the rise is lower as the Marangoni number increases. From Fig. 7(e) and (f), we can observe that the rise velocity and kinetic energy in the drop increases rapidly initially due to the force of buoyancy. Once, the viscous and viscoelastic stresses start to dominate flow dynamics, the rise velocity and kinetic energy no longer increases. Further, with increase in the Marangoni number the rise velocity and kinetic energy decreases as the drop rises.

4.3.2. Influence of initial surfactant concentration

To study the influence of initial surfactant concentration on the rising drop dynamics, we consider the base case flow parameters and vary only the initial surfactant concentration C_0 . We consider the following five different cases in this study: (i) clean drop, (ii) $C_0 = 0.1$, (iii) $C_0 = 0.5$, (iv) $C_0 = 1.0$ and (v) $C_0 = 1.5$. Here, the clean drop refers to the case where no insoluble surfactants were used on the interface. Fig. 9(a) presents the drop shape at $t = 20$, while Fig. 9(b) and (c) presents the surfactant concentration profile along the interface at different time instances for the cases $C_0 = 0.1$ and $C_0 = 1.5$. We can observe that the magnitude of increase in the surfactant concentration at the tail end is higher for larger initial surfactant concentrations. Hence, with an increase in the initial surfactant concentration, the drop at the tail end would be pulled up even more due to large gradients in the interfacial tension and the same can be observed in Fig. 9(a). Thus, the diameter

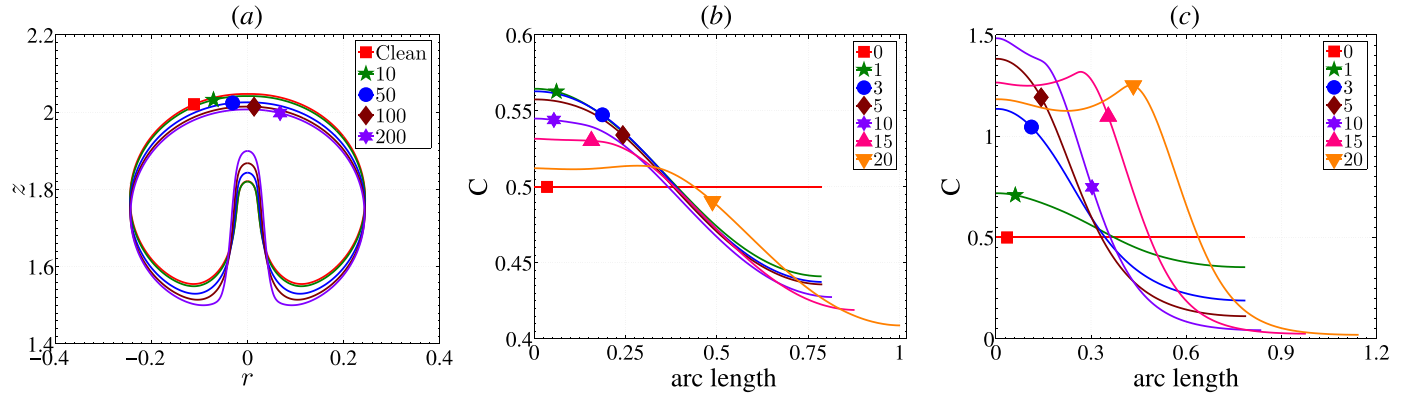


Fig. 10. Influence of Peclet number for a viscoelastic drop rising in a Newtonian fluid column: (a) drop shape at $t = 20$ for different Peclet numbers (i) $Pe = 10$, (ii) $Pe = 50$, (iii) $Pe = 100$ and (iv) $Pe = 200$, surfactant concentration profile along the interface at different time instances for the cases (b) $Pe = 10$ and (c) $Pe = 200$ with flow parameters $Re_2 = 10$, $Fr = 1$, $We = 400$, $Wi_1 = 5$, $\rho_1/\rho_2 = 0.1$, $\epsilon = 2$, $\beta_1 = 0.75$, $\beta_2 = 1.0$, $\alpha_1 = 0.1$, $E = 1$, $C_0 = 0.5$, $C_\infty = 1$, $C_{ref} = 0.5$, $D = 0.5$ and $h_c = 2.5$.

of the drop at the axis of symmetry would decrease as the drop rises because the drop develops an indentation near the tail end. The magnitude of decrease would be larger for higher initial surfactant concentrations as the effect of surfactants would be higher and hence the liquid would move away from low interfacial tension regime. Since, the drop is pulled up more for high surfactant concentrations, the sphericity of the drop would decrease to a larger extent for high initial surfactant concentrations.

4.3.3. Influence of Peclet number

In this section, we study the influence of Peclet number on the viscoelastic drop rising in a Newtonian fluid column with insoluble surfactants on the interface. We consider the base case flow parameters and use the following five different cases: (i) clean drop, (ii) $Pe = 10$, (iii) $Pe = 50$, (iv) $Pe = 100$ and (v) $Pe = 200$. Fig. 10 (a) presents the drop shape at $t = 20$, while Fig. 10(b) and (c) presents the surfactant concentration profile along the interface at different time instances for the cases $Pe = 10$ and $Pe = 200$. We can observe that at high Peclet numbers, the surfactant concentration near the tail end of the drop is much higher compared to low Peclet numbers. This is due to lower diffusion and domination of the transport of the surfactants along the interface for high Peclet numbers. Hence, the effect of surfactants on the rising drop dynamics would be more for higher Peclet numbers. Since, the surfactant concentration is higher near the tail end and also the gradient of the variation of concentration along the interface is high for large Peclet numbers, the drop would be pulled up more at the rear end due to lower interfacial tension and due to the Marangoni convection, the fluid moves away from low interfacial tension regime. This phenomenon can be observed in Fig 10(a). Since, the indentation at the tail end of the drop is higher for larger Peclet numbers, the diameter of the drop at the axis of symmetry would decrease to a larger extent with an increase in the Peclet number. Moreover, the sphericity of the drop would also decrease more with an increase in the Peclet number as the drop deforms more.

4.4. Newtonian drop rise in a viscoelastic fluid column with insoluble surfactants

In this section, we consider a buoyancy driven 3D axisymmetric Newtonian drop rising in a viscoelastic fluid column with insoluble surfactants on the interface. To systematically examine the effects of various flow parameters, we designate a base case which is defined as: $Re_2 = 10$, $Fr = 1$, $We = 400$, $Wi_2 = 15$, $\epsilon = 2$, $\rho_1/\rho_2 = 0.1$, $\beta_1 = 1.0$, $\beta_2 = 0.75$, $\alpha_2 = 0.1$, $Pe = 50$, $C_0 = 0.5$, $C_\infty = 1$, $C_{ref} = 0.5$, $E = 1$, $D = 0.5$ and $h_c = 2.5$. Further, we use 600 degrees of freedom on the interface, the

time step length is set as $\delta t = 0.0005$ and the computations are performed till $I = 16$. Fig. 11 presents the viscoelastic conformation stress profiles at time instances $t = 4, 8$ and 16 . Moreover, the surfactant concentration profile along the interface at different time instances have been presented in Fig. 12.

At time $t = 0$, we assume $\mathbf{u}_0 = 0$ and $\boldsymbol{\tau}_{p,0} = \mathbb{I}$. Initially, the buoyancy force generated by the density difference between two fluids accelerates the drop in the opposite direction of the gravity, i.e. the drop rises up in the bulk fluid column. Further, the motion of the drop is dominated by viscous stresses as the viscoelastic stresses take some time to build up. Along the interface, the interfacial tension force dominates compared to the viscous and viscoelastic stresses. Hence, the shape of the drop is more spherical at $t = 4$. Further, we can observe that the maximum values of viscoelastic stress component τ_{rr} starts to accumulate at the front stagnation point, while τ_{rz} gets built up along the entire circumference of the bubble. However, the maximum values of τ_{zz} are concentrated at the rear stagnation point. At this time still the viscous stresses continue to dominate the flow dynamics as the magnitude of viscoelastic stresses are still small and hence, the drop shape remains more spherical. At time $t = 8$, the drop starts to become prolate and this is an indication that the viscoelastic stresses are starting to dominate the flow dynamics. Further, the maximum values of τ_{zz} and minimum values of τ_{rr} are concentrated at the rear stagnation point. Hence, the polymers near the trailing end of the drop get stretched along the z direction. The extensional viscoelastic stresses in general being large in a thin section at the trailing end of the drop can surmount the interfacial tension, hence forming a cusp-like trailing end [77]. The cusp-like trailing end becomes more and more obvious as the time progresses. Since, the maximum values of τ_{rr} and minimum values of τ_{zz} occur at the front stagnation point, the upstream axial flow experiences a strong turn tangential to the drop surface so that the polymers are greatly extended in the radial directions. Thus, the drop doesn't experience noticeable deformation in the vicinity of its front end. With further advancement in time, the viscoelastic stresses completely dominate the rising drop dynamics. At $t = 16$, τ_{zz} gets concentrated only in the rear stagnation point resulting in the trailing end of the drop being extremely pulled out.

From the surfactant concentration profiles in Fig. 12, we can observe that the concentration near the tail end of the drop increases till $t = 8$, while at the top end it decreases compared to the initial concentration. Due to this, the drop near the tail end has lower interfacial tension while at the top end it has higher interfacial tension. Thus, the drop is easily deformable at the tail end due to the addition of surfactants. Further, Marangoni convection occurs due to non-uniform distribution of surfactant along the interface. Due to the Marangoni

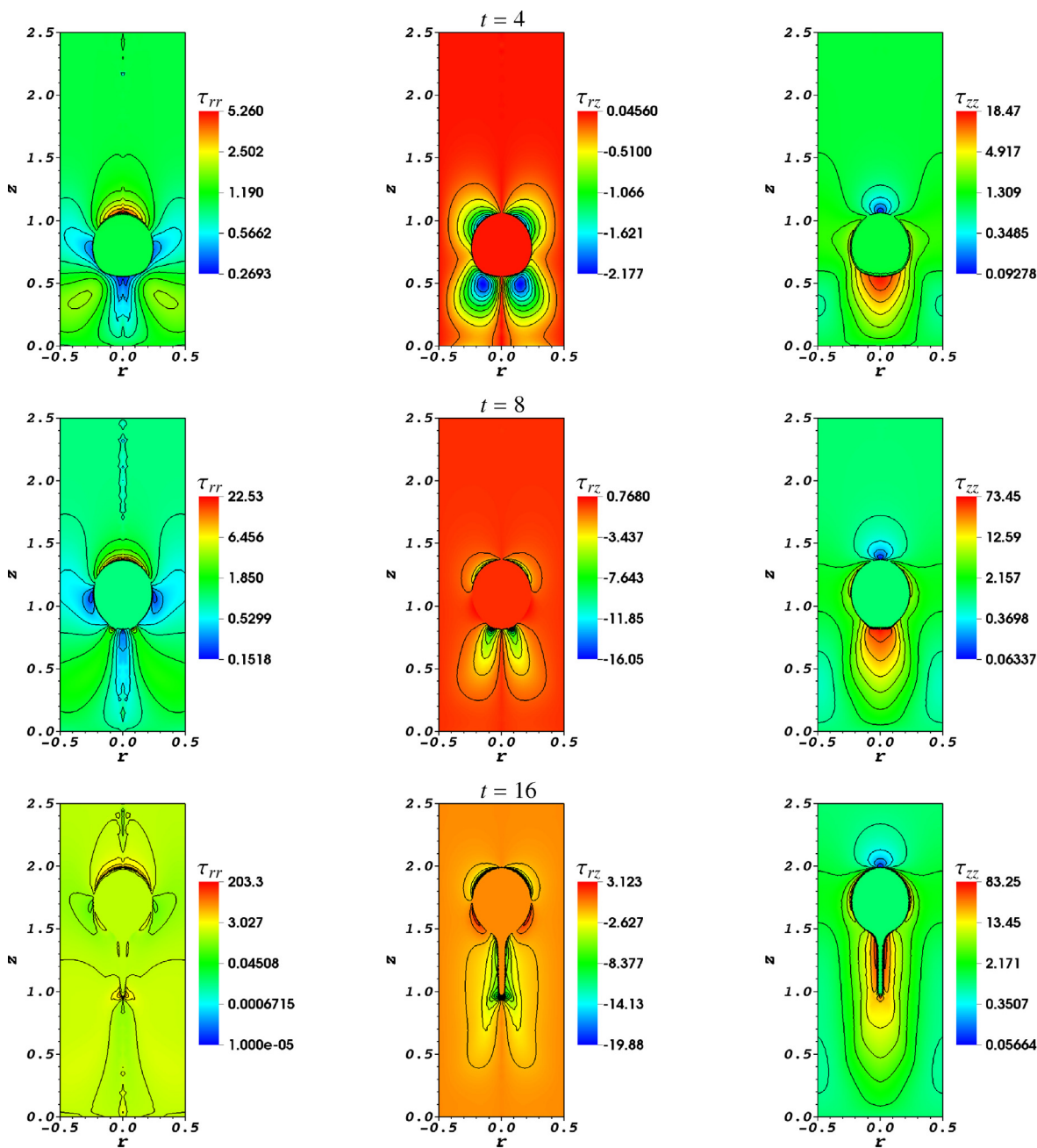


Fig. 11. Viscoelastic conformation stress profiles for a Newtonian drop rising in a viscoelastic fluid column with insoluble surfactants on the interface with flow parameters $Re_2 = 10$, $Fr = 1$, $We = 400$, $Wi_2 = 15$, $\rho_1/\rho_2 = 0.1$, $\epsilon = 2$, $\beta_1 = 1.0$, $\beta_2 = 0.75$, $\alpha_2 = 0.1$, $Pe = 50$, $C_0 = 0.5$, $C_\infty = 1$, $C_{ref} = 0.5$, $E = 1$, $D = 0.5$ and $h_c = 2.5$ at dimensionless times $t = 4, 8$ and 16 .

convection, the fluid inside the drop near the tail end moves away from low interfacial tension regime and hence the drop is pulled up slightly.

Computations of a Newtonian drop rising in a viscoelastic fluid column have revealed an interesting flow phenomenon. In the wake of the rising drop, the velocity field at the vicinity of the trailing end is in the direction of the motion of the drop, whereas it reverses its direction at a small distance away from the trailing end, commonly known as negative wake [78]. Fig. 13 depicts the negative wake phenomenon for the base case flow parameters at time $t = 16$. Moreover, with the addition of insoluble surfactants on the interface, the negative wake is observed much earlier than drops without insoluble surfactants. Further, we didn't observe any jump in the velocity profiles as reported

in the literature [79,80]. We next perform a parametric study to examine the effects of Marangoni number, initial surfactant concentration and Peclet number on the rising drop dynamics in a viscoelastic fluid column.

4.4.1. Influence of Marangoni number

To study the influence of Marangoni number on the rising drop dynamics, we consider the base case flow parameters and vary only the Marangoni number E . The following five different Marangoni numbers are used in this study: (i) $E = 0$, (ii) $E = 0.1$, (iii) $E = 1.0$, (iv) $E = 2.0$, (v) $E = 3.0$. The case $E = 0$ represents the clean case, i.e. no surfactants on the interface. Fig. 14 presents the drop shape at $t = 20$, diameter of the drop at $r = 0$, sphericity, elastic energy, rise velocity and kinetic energy

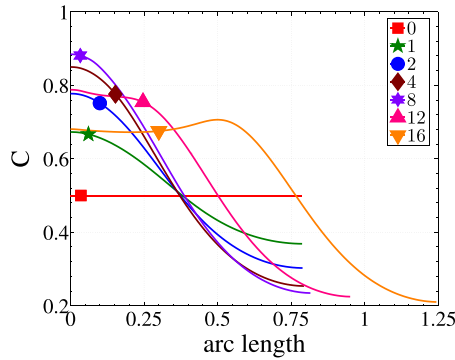


Fig. 12. Surfactant concentration profile along the interface for a Newtonian drop rising in a viscoelastic fluid column at time instances $t = 0, 1, 2, 4, 8, 12$ and 16 for the base case with flow parameters $Re_2 = 10, Fr = 1, We = 400, Wi_2 = 15, \rho_1/\rho_2 = 0.1, \epsilon = 2, \beta_1 = 1.0, \beta_2 = 0.75, \alpha_2 = 0.1, Pe = 50, C_0 = 0.5, C_\infty = 1, C_{ref} = 0.5, E = 1, D = 0.5$ and $h_c = 2.5$.

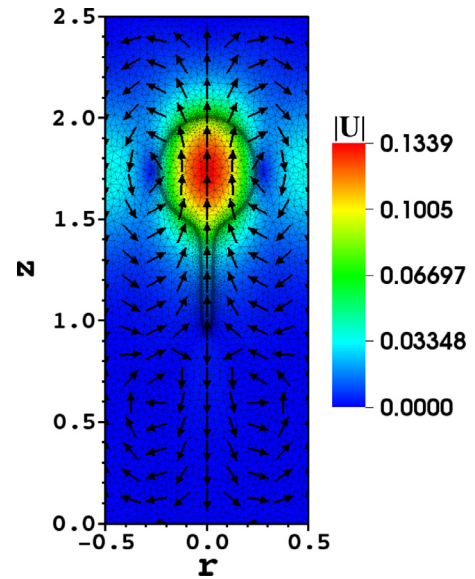


Fig. 13. Magnitude of velocity profile and velocity vectors at dimensionless time $t = 16$ for the base case with flow parameters $Re_2 = 10, Fr = 1, We = 400, Wi_2 = 15, \rho_1/\rho_2 = 0.1, \epsilon = 2, \beta_1 = 1.0, \beta_2 = 0.75, \alpha_2 = 0.1, Pe = 50, C_0 = 0.5, C_\infty = 1, C_{ref} = 0.5, E = 1, D = 0.5$ and $h_c = 2.5$.

in the drop for different Marangoni numbers. Further, Fig. 15 presents the surfactant concentration profile at different time instances for the cases $E = 0.1$ and $E = 3.0$.

We can observe that the concentration of surfactants increase near the tail end of the drop till $t = 7$, afterwards it decreases. Near the top end of the drop, the surfactant concentration decreases with time. From Fig. 15, we can notice that the increase in the surfactant concentration near the top end of the drop is much higher for low Marangoni numbers. We know from the base case study, that a Newtonian drop rising in a viscoelastic fluid column develops a long and narrow tail as the

drop rises. However, due to Marangoni convection we have observed that the drop at the tail end gets pulled up slightly due to the influence of surfactants. Further, the drop at the tail end also becomes much flatter as well and the same can be observed in Fig. 14(a). Since the

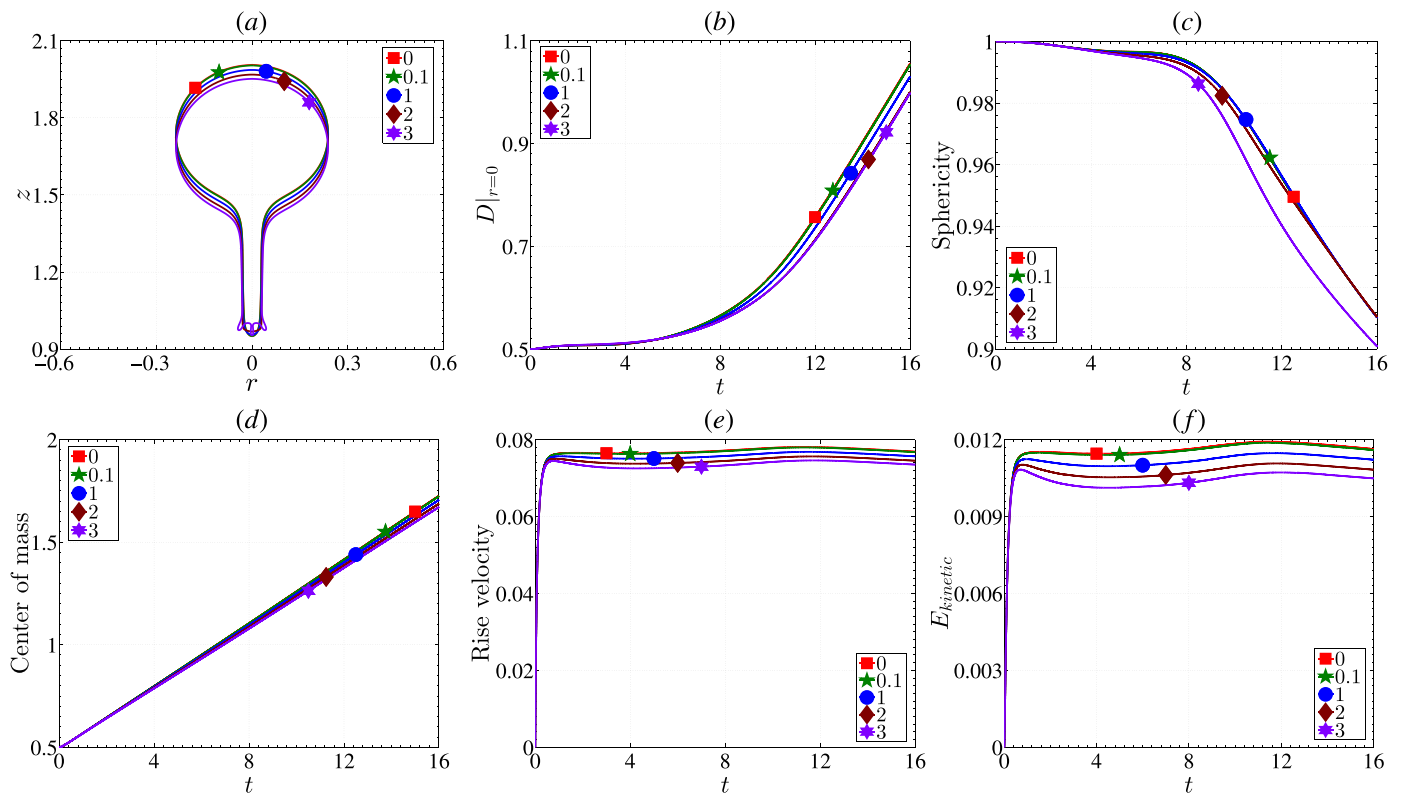


Fig. 14. Influence of Marangoni number for a Newtonian drop rising in a viscoelastic fluid column: (a) drop shape at $t = 16$, (b) diameter of the drop at $r = 0$, (c) sphericity, (d) center of mass, (e) rise velocity and (f) kinetic energy for different Marangoni numbers (i) $E = 0$, (ii) $E = 0.1$, (iii) $E = 1$, (iv) $E = 2$ and (v) $E = 3$ with flow parameters $Re_2 = 10, Fr = 1, We = 400, Wi_2 = 15, \rho_1/\rho_2 = 0.1, \epsilon = 2, \beta_1 = 1.0, \beta_2 = 0.75, \alpha_2 = 0.1, C_0 = 0.5, C_\infty = 1, C_{ref} = 0.5, Pe = 50$ and $D = 0.5$.

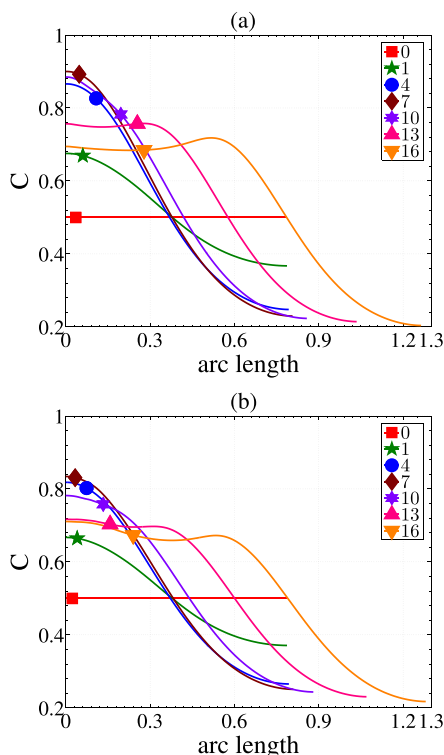


Fig. 15. Surfactant concentration profile along the interface for a Newtonian drop rising in a viscoelastic fluid column at different time instances for the cases (a) $E = 0.1$ and (b) $E = 3.0$.

drop is pulled up due to Marangoni convection, the diameter of the drop at the axis of symmetry increases to a lesser extent compared to a drop rise without surfactants, see Fig. 14(b). The sphericity of the drop decreases with time as the drop deforms due to the effects of viscoelasticity and surfactant migration. The decrease is much larger for the case $E = 3$ as the drop develops small projections at the tail end. The effects of surfactants leads to flatter tail, whereas the viscoelasticity tries to prevent the drop to rise at the tail end and hence, we observe a combination of flat and sharper tail, see Fig. 14(a). Further, the rise velocity and kinetic energy in the drop decreases beyond the initial acceleration due to buoyancy. The decrease in rise velocity and kinetic energy is much more for higher Marangoni numbers. Since, the drop with

higher Marangoni numbers has lower rise velocity, the drop will have a lower center of mass as it rises slowly and the same can be observed in Fig. 14(d).

4.4.2. Influence of initial surfactant concentration

In this section, we study the influence of initial surfactant concentration on the Newtonian drop rising in a viscoelastic fluid column with insoluble surfactants on the interface. We consider the base case flow parameters and use the following five different cases: (i) clean bubble, (ii) $C_0 = 0.25$, (iii) $C_0 = 0.5$, (iv) $C_0 = 1.0$, (v) $C_0 = 1.5$. Fig. 16(a) presents the drop shape at $t = 16$ for all the five cases, while Fig. 16(b) and (c) presents the surfactant concentration profiles along the interface for the cases $C_0 = 0.25$ and $C_0 = 1.5$.

For larger initial surfactant concentrations, we can observe that the magnitude of increase in the surfactant concentration at the tail end of the drop is higher. Hence, the drop at the tail end would be pulled up compared to a drop rise without surfactants, due to Marangoni convection as a result of larger gradients in the interfacial tension and the same is observed in Fig. 16(a). The diameter of the drop will increase due to the effects of viscoelasticity. However, due to the presence of insoluble surfactants, the increase would be lesser as the surfactants tries to pull the tail end of drop up while the viscoelasticity resists it. Thus, the sphericity of the drop would decrease to a larger extent for high surfactant concentrations as the deformation is larger for the highest surfactant concentration.

4.4.3. Influence of Peclet number

To study the influence of Peclet number on the rising drop dynamics, we consider the base case flow parameters and vary only the Peclet number. We consider the following five different cases in this study: (i) clean drop, (ii) $Pe = 10$, (iii) $Pe = 50$, (iv) $Pe = 100$ and (v) $Pe = 125$. Fig. 17(a) presents the drop shape at $t = 16$ for all the five cases, while Fig. 17(b) and (c) presents the surfactant concentration profiles along the interface for the cases $Pe = 10$ and $Pe = 125$.

Flows with high Peclet number have lower diffusion and hence the convection dominates which eventually leads to greater migration of surfactants along the interface. Thus, at high Peclet numbers the surfactant concentration near the tail end of the drop is much higher compared to low Peclet numbers. Due to greater migration of surfactants, the Marangoni convection would be higher as a result of higher gradients in the surfactant concentration along the interface. Hence, the drop would be pulled up more at high Peclet numbers and the same is observed in Fig. 17(a). Further, due to the above phenomenon the increase in the diameter of the bubble at the axis of symmetry would be lesser for high Peclet numbers. Moreover, the sphericity would decrease in time as the

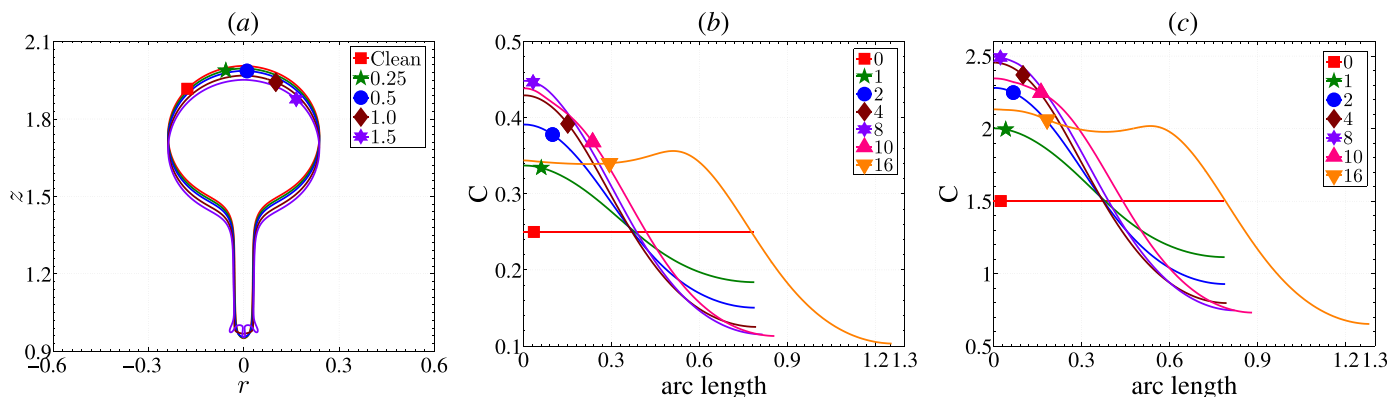


Fig. 16. Influence of initial surfactant concentration for a Newtonian drop rising in a viscoelastic fluid column: (a) drop shape at $t = 16$ for different initial surfactant concentrations (i) $C_0 = 0.25$, (ii) $C_0 = 0.5$, (iii) $C_0 = 1.0$ and (iv) $C_0 = 1.5$, surfactant concentration profile along the interface at different time instances for the cases (b) $C_0 = 0.25$ and (c) $C_0 = 1.5$. with flow parameters $Re_2 = 10$, $Fr = 1$, $We = 400$, $Wi_2 = 15$, $\rho_1/\rho_2 = 0.1$, $\epsilon = 2$, $\beta_1 = 1.0$, $\beta_2 = 0.75$, $\alpha_2 = 0.1$, $E = 1$, $Pe = 50$, $D = 0.5$ and $h_c = 2.5$.

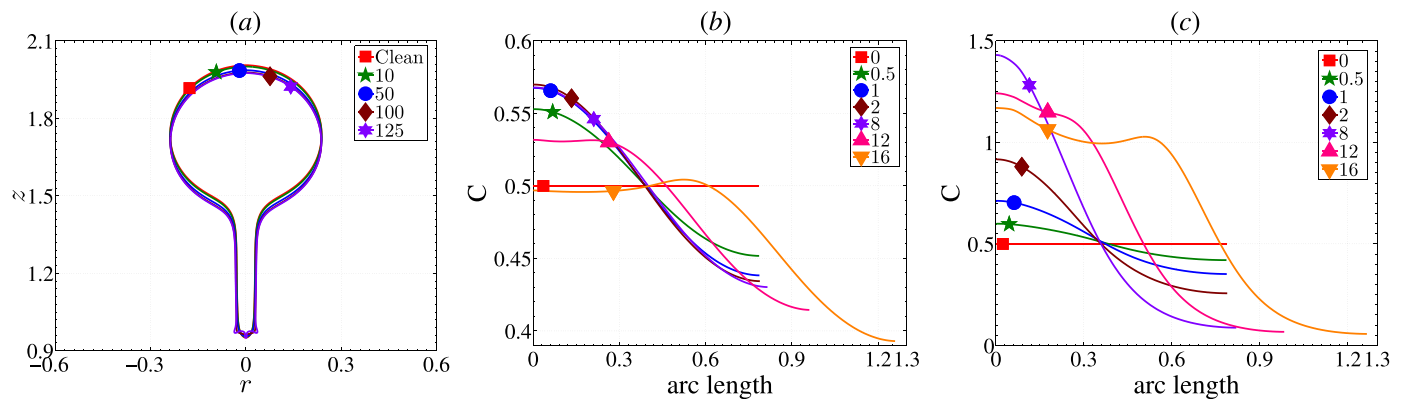


Fig. 17. Influence of Peclet number for a Newtonian drop rising in a viscoelastic fluid column: (a) drop shape at $t = 16$ for different Peclet numbers (i) $Pe = 10$, (ii) $Pe = 50$, (iii) $Pe = 100$ and (iv) $Pe = 125$, surfactant concentration profile along the interface at different time instances for the cases (b) $Pe = 10$ and (c) $Pe = 125$ with flow parameters $Re_2 = 10$, $Fr = 1$, $We = 400$, $Wi_1 = 15$, $\rho_1/\rho_2 = 0.1$, $\epsilon = 2$, $\beta_1 = 1.0$, $\beta_2 = 0.75$, $\alpha_2 = 0.1$, $E = 1$, $C_0 = 0.5$, $C_\infty = 1$, $C_{ref} = 0.5$, $D = 0.5$ and $h_c = 2.5$.

drop deforms and the decrease would be much greater for high Peclet numbers.

5. Summary and observations

A stabilized finite element scheme based on Local Projection Stabilization and coupled ALE and Lagrangian approach is presented for computations of buoyancy driven 3D-axisymmetric viscoelastic two-phase flows with insoluble surfactants. The Navier–Stokes equations, Giesekus constitutive equation and surface evolution equation for the surfactant concentration are solved using this numerical scheme. In this scheme, the surface partial differential equation describing the surfactant concentration on the interface is treated in a Lagrangian manner, whereas all other equations are handled with the arbitrary Lagrangian–Eulerian approach. The mesh update of the moving meshes is realized by solving the linear elasticity equation. The tangential gradient operator technique is used to handle the curvature term semi-implicitly in the force balance at the interface. This technique allows us to approximate the curvature term with continuous finite element basis functions. The main highlight of the numerical scheme is the three-field local projection stabilization formulation. One-level LPS scheme based on an enriched approximation space and a discontinuous projection space is used in the stabilized formulation. This stabilized numerical scheme allowed us to use isoparametric second order conforming finite elements enriched with cubic bubble functions for velocity and viscoelastic stress, second order finite elements for surfactant concentration and discontinuous first order finite element for pressure. First order implicit Euler method is used for time discretization and fixed point iteration is used for linearization of the non-linear terms in the equations. An excellent mass conservation of the fluid mass and of the total surfactant mass is obtained with the proposed scheme.

A grid independence study is performed to obtain grid independent numerical solutions. Further, the numerical scheme is validated for a Newtonian drop rising in a Newtonian/Giesekus fluid column using the numerical results in the literature. Further, a comprehensive numerical investigation is performed for a Newtonian drop rising in a viscoelastic fluid column and a viscoelastic drop rising in a Newtonian fluid column with insoluble surfactants on the interface. The effects of the Marangoni number, initial surfactant concentration and Peclet number on the rising drop dynamics are analyzed. The observations are summarized as follows. A viscoelastic drop rising in a Newtonian fluid column develops an indentation around the rear stagnation point with a dimpled shape. Moreover, surfactants on the interface force the drop to rise slowly but increases the indentation, i.e. the drop is pulled up more at the tail end. Further, a Newtonian drop rising in a viscoelastic fluid column experiences an extended trailing edge with a cusp-like shape and the negative

wake phenomenon is observed. The presence of surfactants pulls the tail end of the drop up slightly compared to flows without surfactants and makes the tail flatter with/without small undulations depending on the magnitude of the surfactant concentrations. The proposed numerical scheme shall be used to analyze the amount of polymers and surfactants to be used during polymer flooding process for maximizing the oil and gas recovery [1–3].

Acknowledgments

The work of Jagannath Venkatesan is supported by the [Tata Consultancy Services-pl2X-sim-\(TCS\)](#), India through the TCS Research Scholarship Program.

Supplementary material

Supplementary material associated with this article can be found, in the online version, at doi:10.1016/j.jnnfm.2019.04.002.

References

- [1] J. Hou, Z. Liu, S. Zhang, X. Yue, J. Yang, The role of viscoelasticity of alkali/surfactant/polymer solutions in enhanced oil recovery, *J. Petrol. Sci. Eng.* 47 (2005) 219–235.
- [2] J. van Santvoort, M. Golombok, Viscoelastic surfactants for diversion control in oil recovery, *J. Petrol. Sci. Eng.* 135 (2015) 671–677.
- [3] J. van Santvoort, M. Golombok, Improved oil reservoir sweep with viscoelastic surfactants, *Energy Fuels* 30 (11) (2016) 9226–9232.
- [4] J.G. Oldroyd, On the formulation of rheological equations of state, *Proc. R. Soc. Lond.* 200 (1950) 523–541.
- [5] H. Giesekus, A simple constitutive equation for polymeric fluids based on the concept of deformation-dependent tensorial mobility, *J. Non-Newton. Fluid Mech.* 11 (1982) 69–109.
- [6] R.B. Bird, P.J. Dotson, N.L. Johnson, Polymer solution rheology based on a finitely extensible bead-spring chain model, *J. Non-Newton. Fluid Mech.* 7 (1980) 213–235.
- [7] M.D. Chilcott, J.M. Rallison, Creeping flow of dilute polymer solutions past cylinders and spheres, *J. Non-Newton. Fluid Mech.* 29 (1988) 381–432.
- [8] N.P. Thien, R.I. Tanner, A new constitutive equation derived from network theory, *J. Non-Newton. Fluid Mech.* 2 (1977) 353–365.
- [9] W.M.H. Verbeeten, G.W.M. Peters, F.P.T. Baaijens, Differential constitutive equations for polymer melts: the extended Pom-Pom model, *J. Rheol.* 45 (4) (2001) 823–843.
- [10] H.A. Stone, A simple derivation of the time-dependent convection-diffusion equation for surfactant transport along a deforming interface, *Phys. Fluids A* 2 (1) (1990) 111–112.
- [11] H. Wong, D. Rumschitzki, C. Maldarelli, On the surfactant mass balance at a deforming fluid interface, *Phys. Fluids* 8 (1996) 3203–3204.
- [12] A.J. James, J. Lowengrub, A surfactant-conserving volume-of-fluid method for interfacial flows with insoluble surfactant, *J. Comput. Phys.* 201 (2004) 685–722.
- [13] Y.Y. Renardy, M. Renardy, V. Cristini, A new volume-of-fluid formulation for surfactants and simulations of drop deformation under shear at a low viscosity ratio, *Eur. J. Mech. – B/Fluids* 21 (2002) 49–59.
- [14] J.-J. Xu, Z. Li, J. Lowengrub, H. Zhao, A level-set method for interfacial flows with surfactant, *J. Comput. Phys.* 212 (2006) 590–616.

- [15] W.C. de Jesus, A.M. Roma, M.R. Pivello, M.M. Villar, A. da Silveira-Neto, A 3D front-tracking approach for simulation of a two-phase fluid with insoluble surfactant, *J. Comput. Phys.* 281 (2015) 403–420.
- [16] M. Muradoglu, G. Tryggvason, Simulations of soluble surfactants in 3D multiphase flow, *J. Comput. Phys.* 274 (2014) 737–757.
- [17] I.B. Bazhlekov, P.D. Anderson, H.E.H. Meijer, Numerical investigation of the effect of insoluble surfactants on drop deformation and breakup in simple shear flow, *J. Colloid Interface Sci.* 298 (2006) 369–394.
- [18] C.D. Eggleton, T.-M. Tsai, K.J. Stebe, Tip streaming from a drop in the presence of surfactants, *Phys. Rev. Lett.* 87 (4) (2001) 048302.
- [19] S. Yon, C. Pozrikidis, A finite-volume/boundary-element method for flow past interfaces in the presence of surfactants, with application to shear flow past a viscous drop, *Comput. Fluids* 27 (8) (1998) 879–902.
- [20] M.-C. Lai, Y.-H. Tseng, H. Huang, An immersed boundary method for interfacial flows with insoluble surfactant, *J. Comput. Phys.* 227 (2008) 7279–7293.
- [21] M.-C. Lai, C. Huang, Y. Huang, Simulating the axisymmetric interfacial flows with insoluble surfactant by immersed boundary method, *Int. J. Numer. Anal. Model.* 8 (1) (2011) 105–117.
- [22] J. Lee, C. Pozrikidis, Effect of surfactants on the deformation of drops and bubbles in Navier–Stokes flow, *Comput. Fluids* 35 (2006) 43–60.
- [23] S. Engblom, M. Do-Quang, G. Amberg, A. Tornberg, On diffuse interface modeling and simulation of surfactants in two-phase fluid flow, *Commun. Comput. Phys.* 14 (4) (2013) 879–915.
- [24] K.E. Teigen, P. Song, J. Lowengrub, A. Vogit, A diffuse-interface method for two-phase flows with soluble surfactants, *J. Comput. Phys.* 230 (2011) 375–393.
- [25] S. Ganesan, L. Tobiska, Arbitrary Lagrangian–Eulerian finite-element method for computation of two-phase flows with soluble surfactants, *J. Comput. Phys.* 231 (9) (2012) 3685–3702.
- [26] S. Khatri, A.-K. Tornberg, A numerical method for two phase flows with insoluble surfactants, *Comput. Fluids* 49 (2011) 150–165.
- [27] S. Khatri, A.-K. Tornberg, An embedded boundary method for soluble surfactants with interface tracking for two-phase flows, *J. Comput. Phys.* 256 (2014) 768–790.
- [28] M. Booty, M. Siegel, A hybrid numerical method for interfacial fluid flow with soluble surfactant, *J. Comput. Phys.* 229 (10) (2010) 3864–3883.
- [29] S. Shin, J. Chergui, D. Juric, L. Kahouadji, O.K. Matar, R.V. Craster, A hybrid interface tracking - level set technique for multiphase flow with soluble surfactant, *J. Comput. Phys.* 359 (2018) 409–435.
- [30] S. Adami, X. Hu, N. Adams, A conservative SPH method for surfactant dynamics, *J. Comput. Phys.* 229 (5) (2010) 1909–1926.
- [31] T. Chinyoka, Y.Y. Renardy, M. Renardy, D.B. Khismatullin, Two-dimensional study of drop deformation under simple shear for Oldroyd-B liquids, *J. Non-Newton. Fluid Mech.* 130 (2005) 45–56.
- [32] F. Habla, H. Marschall, O. Hinrichsen, L. Dietsche, H. Jasak, J.L. Favero, Numerical simulation of viscoelastic two-phase flows using openFOAM, *Chem. Eng. Sci.* 66 (2011) 5487–5496.
- [33] D.J.E. Harvie, J.J. Cooper-White, M.R. Davidson, Deformation of a viscoelastic droplet passing through a microfluidic contraction, *J. Non-Newton. Fluid Mech.* 155 (2008) 67–79.
- [34] S.B. Pillapakam, P. Singh, A level-set method for computing solutions to viscoelastic two-phase flow, *J. Comput. Phys.* 174 (2001) 552–578.
- [35] S.B. Pillapakam, P. Singh, D. Blackmore, N. Aubry, Transient and steady state of a rising bubble in a viscoelastic fluid, *J. Fluid Mech.* 589 (2007) 215–252.
- [36] P. Yue, J.J. Feng, C. Liu, J. Shen, Diffuse-interface simulations of drop coalescence and retraction in viscoelastic fluids, *J. Non-Newton. Fluid Mech.* 129 (2005) 163–176.
- [37] P. Yue, C. Zhou, J.J. Feng, C.F. Ollivier-Gooch, H.H. Hu, Phase-field simulations of interfacial dynamics in viscoelastic fluids using finite elements with adaptive meshing, *J. Comput. Phys.* 219 (2006) 47–67.
- [38] Y. Zhang, H. Wang, T. Tang, Simulating two-phase viscoelastic flows using moving finite element methods, *Commun. Comput. Phys.* 7 (2) (2010) 333–349.
- [39] C. Chung, M.A. Hulsen, J.M. Kim, K.H. Ahn, S.J. Lee, Numerical study on the effect of viscoelasticity on drop deformation in simple shear and 5:1:5 planar contraction/expansion microchannel, *J. Non-Newton. Fluid Mech.* 155 (2008) 80–93.
- [40] C. Chung, J.M. Kim, M.A. Hulsen, K.H. Ahn, S.J. Lee, Effect of viscoelasticity on drop dynamics in 5:1:5 contraction/expansion microchannel flow, *Chem. Eng. Sci.* 64 (2009) 4515–4524.
- [41] S. Mukherjee, K. Sarkar, Effects of viscoelasticity on the retraction of a sheared drop, *J. Non-Newton. Fluid Mech.* 165 (2010) 340–349.
- [42] S. Mukherjee, K. Sarkar, Viscoelastic drop falling through a viscous medium, *Phys. Fluids* 23 (2011) 013101.
- [43] D. Izbassarov, M. Muradoglu, A front-tracking method for computational modeling of viscoelastic two-phase flow systems, *J. Non-Newton. Fluid Mech.* 223 (2015) 122–140.
- [44] D. Izbassarov, M. Muradoglu, A computational study of two-phase viscoelastic systems in a capillary tube with a sudden contraction/expansion, *Phys. Fluids* 28 (2016) 012110.
- [45] J. Venkatesan, S. Ganesan, Local projection stabilized finite element modeling of viscoelastic two-phase flows, arXiv:1902.06466 (2019) 1–31.
- [46] S.J. Lind, T.N. Phillips, The effect of viscoelasticity on a rising gas bubble, *J. Non-Newton. Fluid Mech.* 165 (2010) 852–865.
- [47] M.J. Walters, T.N. Phillips, A non-singular boundary element method for modelling bubble dynamics in viscoelastic fluids, *J. Non-Newton. Fluid Mech.* 235 (2016) 109–124.
- [48] S. Ganesan, G. Matthies, L. Tobiska, On spurious velocities in incompressible flow problems with interfaces, *Comput. Methods Appl. Mech. Eng.* 196 (7) (2007) 1193–1202.
- [49] A.N. Brooks, T.J.R. Hughes, Streamline upwind/Petrov–Galerkin formulations for convection dominated flows with particular emphasis on the incompressible Navier–Stokes equations, *Comput. Methods Appl. Mech. Eng.* 32 (1982) 199–259.
- [50] R. Guenette, M. Fortin, A new mixed finite element method for computing viscoelastic flows, *J. Non-Newton. Fluid Mech.* 60 (1995) 27–52.
- [51] A. Fortin, R. Guenette, R. Pierre, On the discrete EVSS method, *Comput. Methods Appl. Mech. Eng.* 189 (1) (2000) 121–139.
- [52] M. Fortin, A. Fortin, A new approach for the FEM simulation of viscoelastic flows, *J. Non-Newton. Fluid Mech.* 32 (1989) 295–310.
- [53] O.M. Coronado, D. Arora, M. Behr, M. Pasquali, Four-field Galerkin/least-squares formulation for viscoelastic fluids, *J. Non-Newton. Fluid Mech.* 140 (1–3) (2006) 132–144.
- [54] R. Fattal, R. Kupferman, Time-dependent simulation of viscoelastic flows at high Weissenberg number using the log-conformation representation, *J. Non-Newton. Fluid Mech.* 126 (2005) 23–37.
- [55] J. Kwack, A. Masud, A three-field formulation for incompressible viscoelastic fluids, *Int. J. Eng. Sci.* 48 (11) (2010) 1413–1432.
- [56] E. Castillo, R. Codina, Variational multi-scale stabilized formulations for the stationary three-field incompressible viscoelastic flow problem, *Comput. Methods Appl. Mech. Eng.* 279 (2014) 579–605.
- [57] J. Venkatesan, S. Ganesan, A three-field local projection stabilized formulation for computations of Oldroyd-B viscoelastic fluid flows, *J. Non-Newton. Fluid Mech.* 247 (2017) 90–106.
- [58] S. Ganesan, Simulations of impinging droplets with surfactant-dependent dynamic contact angle, *J. Comput. Phys.* 301 (2015) 178–200.
- [59] C. Pozrikidis, A finite-element method for interfacial surfactant transport, with application to the flow-induced deformation of a viscous drop, *J. Eng. Math.* 49 (2004) 163–180.
- [60] S. Ganesan, L. Tobiska, An accurate finite element scheme with moving meshes for computing 3D-axisymmetric interface flows, *Int. J. Numer. Methods Fluids* 57 (2) (2008) 119–138.
- [61] S. Hysing, S. Turek, D. Kuzmin, N. Parolini, E. Burman, S. Ganesan, L. Tobiska, Quantitative benchmark computations of two-dimensional bubble dynamics, *Int. J. Numer. Methods Fluids* 60 (2009) 1259–1288.
- [62] J. Venkatesan, S. Ganesan, Computational modeling of impinging viscoelastic droplets, *J. Non-Newton. Fluid Mech.* 263 (2019) 42–60.
- [63] J.R. Shewchuk, Triangle: Engineering a 2D Quality Mesh Generator and Delaunay Triangulator, in: M.C. Lin, D. Manocha (Eds.), Applied Computational Geometry: Towards Geometric Engineering, Lecture Notes in Computer Science, 1148, Springer-Verlag, 1996, pp. 203–222. From the First ACM Workshop on Applied Computational Geometry
- [64] J.R. Shewchuk, Delaunay refinement algorithms for triangular mesh generation, *Comput. Geometry* 22 (1–3) (2002) 21–74.
- [65] R. Becker, M. Braack, A finite element pressure gradient stabilization for the Stokes equations based on local projections, *Calcolo* 38 (2001) 173–199.
- [66] R. Becker, M. Braack, A Two-Level Stabilization Scheme for the Navier–Stokes Equations, in: M. Feistauer, V. Dolejší, P. Knobloch, K. Najzar (Eds.), Numerical Mathematics and Advanced Applications, Springer Berlin Heidelberg, 2004, pp. 123–130.
- [67] M. Braack, E. Burman, Local projection stabilization for the Oseen problem and its interpretation as a variational multiscale method, *SIAM J. Numer. Anal.* 43 (6) (2006) 2544–2566.
- [68] G. Matthies, P. Skrzypacz, L. Tobiska, A unified convergence analysis for local projection stabilisations applied to the Oseen problem, *ESAIM Math. Modell. Numer. Anal.* 41 (4) (2007) 713–742.
- [69] S. Ganesan, G. Matthies, L. Tobiska, Local projection stabilization of equal order interpolation applied to the Stokes problem, *Math. Comput.* 77 (264) (2008) 2039–2060.
- [70] S. Ganesan, L. Tobiska, Stabilization by local projection for convection-diffusion and incompressible flow problems, *J. Scient. Comput.* 43 (3) (2010) 326–342.
- [71] J.W. Barrett, H. Garcke, R. Nürnberg, Eliminating spurious velocities with a stable approximation of viscous incompressible two-phase Stokes flow, *Comput. Methods Appl. Mech. Eng.* 267 (2013) 511–530.
- [72] E. Bänsch, Finite element discretization of the Navier–Stokes equations with a free capillary surface, *Numerische Mathematik* 88 (2001) 203–235.
- [73] P.R. Amestoy, I.S. Duff, J.-Y. L'Excellent, J. Koster, A fully asynchronous multi-frontal solver using distributed dynamic scheduling, *SIAM J. Matrix Anal. Appl.* 23 (1) (2001) 15–41.
- [74] P.R. Amestoy, A. Guermouche, J.-Y. L'Excellent, S. Pralet, Hybrid scheduling for the parallel solution of linear systems, *Parallel Comput.* 32 (2) (2006) 136–156.
- [75] U. Willbrandt, C. Bartsch, N. Ahmed, N. Alia, F. Anker, L. Blank, A. Caiazzo, S. Ganesan, S. Giere, G. Matthies, R. Meesala, A. Shamim, J. Venkatesan, V. John, ParMoon - a modernized program package based on mapped finite elements, *Comput. Math. Appl.* 74 (1) (2017) 74–88.
- [76] M. Vahabi, B. Kamkari, Simulating gas bubble shape during its rise in a confined polymeric solution by WC-SPH, *Eur. J. Mech. / B Fluids* 75 (2019) 1–14.
- [77] Y.J. Liu, T.Y. Liao, D.D. Joseph, A two-dimensional cusp at the trailing edge of an air bubble rising in a viscoelastic liquid, *J. Fluid Mech.* 304 (1995) 321–342.
- [78] O. Hassager, Negative wake behind bubbles in non-newtonian liquids, *Nature* 279 (1979) 402–403.
- [79] E. Soto, C. Goujon, R. Zenit, O. Manero, A study of velocity discontinuity for single air bubbles rising in an associative polymer, *Phys. Fluids* 18 (2006) 121510.
- [80] J.R. Herrera-Velarde, R. Zenit, D. Chehata, B. Mena, The flow of non-Newtonian fluids around bubbles and its connection to the jump discontinuity, *J. Non-Newton. Fluid Mech.* 111 (2003) 199–209.